Free-fall experiments of volcanic ash particles using a 2D video disdrometer

Sung-Ho Suh[1] (Email: suhsh1215@pukyong.ac.kr)

Masayuki Maki[2*] (Email: maki@gm.kagoshima-u.ac.jp)

Masato Iguchi[3] (Email: iguchi@svo.dpri.kyoto-u.ac.jp)

Dong-In Lee[1] (Email: leedi@pknu.ac.kr)

Akihiko Yamaji[4] (Email: yamaji@jwa.or.jp)

Tatsuya Momotani[4] (Email: momotani@ jwa.or.jp)

Institutional addresses:

[1]Department of Environmental Atmospheric Sciences, Pukyong National University, Namgu, Busan, Republic of Korea

[2]Research and Education Center for Natural Hazards, Kagoshima University, Korimoto, Kagoshima, Japan

[3]Sakurajima Volcano Research Center, Disaster Prevention Research Institute, Kyoto University, Sakurajima, Kagoshima, Japan

[4]Japan Weather Association, Higashi-Ikebukuro, Toshima-ku, Tokyo, Japan

* Corresponding author: Masayuki Maki, (maki@gm.kagoshima-u.ac.jp)

Key Points: Volcanic ash, 2DVD, aerodynamic properties, laboratory experiments

The English in this document has been checked by at least two professional editors, both native speakers of English. For a certificate, please see:

http://www.textcheck.com/certificate/7pU3Ux

Abstract

Information of aerodynamic parameter of volcanic ash particles, such as terminal velocity, axis ratio, and canting angle, which are necessary for quantitative ash-fall estimations with weather radar. In this study, free-fall experiments of volcanic ash particle were accomplished using a two-dimensional video disdrometer under controlled conditions.

Samples containing a rotating symmetric axis were selected and divided into five types according to shape and orientation: oblate spheroid with horizontal rotating axis (OH), oblate spheroid with vertical axis (OV), prolate spheroid with horizontal rotating axis (PH), prolate spheroid with vertical rotating axis (PV), and sphere (Sp). The horizontally (OH and PH) and vertically (OV and PV) oriented particles were present in proportions of 76% and 22%, and oblate and prolate spheroids were in proportions of 76% and 24%, respectively. The most common shape type was OH (57%).

The terminal velocities of OH, OV, PH, PV and Sp were obtained analyzing 2DVD data. The terminal velocities of PV were highest compared to those of other particle types. The lowest terminal velocities were found in OH particles. It is interesting the terminal velocities for OH decreased rapidly in the range $0.5 < D < 1$ mm corresponding to the decrease in axis ratio (i.e., smaller the particle, the flatter the shape). The axis ratios of all particle types except Sp were found to be converged to 0.94 at $D > 2$ mm.

The histogram of canting angles followed unimodal and bimodal distributions with respect to horizontally and vertically oriented particles, respectively. The mean values and the standard deviation of entire particle shape types were close to 0° and 10°, respectively under calm atmospheric conditions.

47 # 1. Introduction

48 Volcanic eruptions are considered one of the most severe types of natural phenomena, and can lead
49 to human casualties and property damage. Ash consists of very fine-grained fragments, volume-
50 equivalent spherical particle diameter (D in mm) is generally smaller than 2 mm, and these are
51 generally dominated by broken glass shards rather than crystal and lithic fragments. Wilson et al. (2012)
52 overview for the ash effects on critical infrastructures such as ash fall and acid rain. Hilman et al. (2012)
53 investigate the effect ash particles on human health in case of Sakurajima volcanic eruptions. More
54 comprehensive descriptions on the volcanic ash impacts on society is found in Sigurdsson et al. (2015)
55 and Wilson et al. (2015). Following an eruption, fine airborne volcanic ash flows for several tens of
56 kilometers, which can cause major problems by increasing aviation traffic (e.g., Bonadonna et al., 2012;
57 Langmann et al., 2012); this was seen after the eruption of Eyjafjallajökull volcano in Iceland during
58 the period April 14–21, 2010, for example Bonadonna et al. (2011). From the viewpoint of
59 volcanological hazard reduction, accurate description of transport and deposition in the numerical
60 forecasting model of volcanic ash clouds are vitally important (Poulidis et al., 2017).

61 Terminal fall velocity (V_T) of a particle is affected by its shape, density, size, and atmospheric
62 properties. Wilson and Huang (1979), Dellino (2005), and Coltelli et al. (2008) introduced the
63 influence of ash particle shapes on its V_T. Haider and Levenspile (1989) and Ganser (1993) analyzed
64 V_T of volcanic ash particle on the drag coefficient (C_D) which is dependent on the particle shape and
65 atmospheric condition. Transport and sedimentation of volcanic ash are complex processes, and the
66 residence time and fall velocity of ash is critically dependent on particle size (Bonadonna et al., 1998),
67 where with respect to the latter, smaller particles could be flowing in the atmosphere further from the
68 vent.

69 Aerodynamic properties are important for safe aviation, and for studying the effects of volcanic
70 ash on climate change, since these parameters determine the residence time of ash particles in the

atmosphere (e.g., Folch et al., 2009). The V_T of particles vary widely due to their irregular shapes and material components (e.g., Wilson, 1972; Harris and Rose, 1983; Bonadonna et al., 2011, Maki et al., 2016). Bonadonna et al. (2011) analyzed V_T of volcanic ash particle with various particle density (ρ_s) from 990 to 2738 kg m^{-3} and Maki et al. (2016) summarized the list of various V_T relationships suggested by previous studies. Volcanic ash particles have a range of shapes, and this presents a major challenge when analyzing their characteristics. Recently, the irregularity of volcanic ash particles was analyzed in detail based on the features of various regular particles, such as cubes, cylinders, and disks (Bagheri and Bonadonna, 2016), using a computed tomography (CT) scanner (Dioguardi et al., 2017; Garboczi and Bullard, 2017).

There are two approaches to studying these aerodynamic properties. The first approach is theoretical, where a numerical simulation model is used to calculate terminal velocities, drag force, and Reynolds number (Re); examples of this approach can be found in Happel and Brenner (2012). The second approach is related to experimental research, in which the aforementioned relationships are determined experimentally. For instance, Bagheri et al. (2013) and Bagheri and Bonadonna (2016) analyzed the aerodynamic features of irregular shaped ash particle from the free fall experiments. Dioguardi et al. (2018) suggested a new model of fluid drag for irregular shaped particles using various previous researches. Since the aerodynamic feature depends on atmospheric condition and it can affect the retrieval of V_T, it would be suggested that it can be analyzed through the free-fall laboratory experiments for the following main reasons: 1) there is few chance to measure natural falling ash particles. 2) it can be possible to control the size of ash particle in the free fall experiments. 3) and can reduce wind effect in the experiments.

The present study applies the second approach (experimental research) to clarify the physical characteristics of volcanic ash particles analyzing the experimental data. The rest of this paper is organized as follows. Section 2 describes the free-fall experiments of ash particles and methods of

95 analysis. Section 3 presents the results of the free fall experiments. Section 4 is discussions and section
96 5 summarizes the results.
97

2. Data and Methods

a. Two dimensional (2D) video disdrometer

The 2D video disdrometer (2DVD) was developed by Joanneum Research (Graz, Austria) to detect single raindrop particles, and the instrument has been modified to cover the errors caused by turbulence effects (Nešpor et al., 2000). The device is able to observe the shape, V_T, and β of a single particle using optical light. The ability to analyze a single particle is a significant advantage compared to other disdrometers, such as the Joss-Waldvogel disdrometer (Joss and Waldvogel, 1967), the Precipitation Occurrence Sensor System (Sheppard, 1990), and Parsivel (Löffler-Mang and Joss 2000). For instance, Parsivel considers a fixed measurement area without any consideration of particle shape (e.g., Tokay et al., 2014), while 2DVD observes particles by passing them through a 100 cm^2 observation area consisting of two light sources and reflecting mirrors and two cameras, one set 6.2 mm above the other, and collects data with a resolution of 630 pixels; this results in a pixel size of 0.2 mm at 55 kHz (Kruger and Krajewski, 2002). Particles passing through the observation area yield shape information according to the radiation intensity of the light sources, which is helpful for calculation of γ and β. The V_T of particles is calculated using the height difference between the two cameras. Based on these advantages, the oscillation and particle shape of raindrops can be analyzed by 2DVD (Thurai and Bringi, 2005). Böhm (1989) analyzed the aerodynamic properties of an irregular hydrometeor and Huang et al. (2010, 2015) used 2DVD to analyze the features of irregularly shaped snow. There have been few previous aerodynamic analyses of volcanic ash particles performed using 2DVD, which is able to detect and analyze volcanic ash particles with a range of irregular shapes. Thus, 2DVD offers a unique approach as a new observation strategy.

b. Definition of particle shape type

Volcanic ash particles have various shapes that can be detected by 2DVD (Fig. 1). In the case of raindrops, the DSD is dependent upon the break-up and coalescence processes occurring via up and downdrafts, since the forces of gravity and buoyancy can easily affect raindrop shapes (Rosenfeld and Ulbrich, 2003). However, solid particles do not readily change shape when falling without the influence of forces such as collision. It is thus inferred that many particle shapes would be found in the atmosphere, and that it would be possible to define and classify each particle shape type if we were able to accurately detect a single particle. Thus, the range of γ for solid particles would be expected to be wide compared to that of raindrops, and various values of V_T and β would likely be observed. The γ_x of a particle is defined as the ratio of height to width for the observation direction x, and its representative value is calculated using the geometric means of the two γ (γ_1, γ_2) detected by cameras 1 and 2, respectively (Eq. 1):

$$\gamma_{1(2)} = \frac{\mathrm{Height}_{1(2)}}{\mathrm{Width}_{1(2)}}, \qquad \gamma = \sqrt{\gamma_1 \gamma_2}$$

Eq. (1).

The difference in angle between the rotating symmetric axis and vertical axis is defined as β. The counter-clockwise (clockwise) movement of the rotating symmetric axis has a positive (negative) value and the entire range is 180° (from -90° to 90°) with 0° as the center.

It is necessary to consider the true axis ratio (γ_T) to correctly define the particle shape (Fig. 2). The apparent axis ratio (γ_A) considers the effect of β but the γ_T does not. The 2D coordinates (x, z) of the particle shape with β are defined as follows:

145

146 $$x_A = \mathrm{r}\ \cos(\theta + \beta), \qquad z_A = \mathrm{r}\ \sin(\theta + \beta)$$

147

148 $$x_T = \mathrm{r}\ \cos\theta, \qquad z_T = \mathrm{r}\ \sin\theta$$

149

150 where subscript A is the coordinate of the original data coordinate considering the β and subscript
151 T is the modified data coordinate. The symbol r refers to the length from the data point to the center
152 and the symbol θ represents the degrees of data coordinates from the positive x axis, which range
153 between 0° and 180°. In this paper, γ stands for γ_A for convenience.

154 An objective criterion for particle shape type was considered since particle shapes can be highly
155 diverse and irregular (e.g., Bagheri and Bonadonna, 2016; Dioguardi et al., 2017; Garboczi and Bullard,
156 2017; Dioguardi et al., 2018). In the case of irregular particles, the γ can change according to the
157 observation direction; however, any criterion should be able to define the particle shape types strictly
158 and reliably. To solve this problem, particles with a rotating symmetric axis were the main target of
159 the present study. Therefore, we considered oblate spheroid (O), prolate spheroid (P), and sphere (Sp),
160 which all have a rotating symmetric axes. Among these particle types, the major axes of the oblate and
161 prolate spheroids could be horizontally (H) and vertically (V) oriented with respect to the ground,
162 respectively. Thus, the various particle shapes were divided into five types as follows; OH, OV, PH,
163 PV, and Sp.

164 To define these particle shape types, a strict definition of the γ_T is required, which can be calculated
165 from the β. As with the γ, the two β values are automatically calculated by 2DVD. In the case where
166 the β is assumed as 0°, the rotating symmetric axis for OH and PV can be defined, since it is observed
167 for any observation direction parallel to the ground. However, in the case of OV and PH particles, the
168 rotating symmetric axis cannot be defined when the observation direction is parallel. In the case where

169 the β is not 0°, γ_T for all particle shape types would not change when oscillation occurs in a direction
170 orthogonal to the observation direction, but it is difficult to estimate both γ_T and β when particle
171 oscillation appears in a direction parallel to the observation direction. The ability to restore the γ_T and
172 β relative to this observation direction is limited, which is one of the main disadvantages of the 2D
173 observation strategy.

174 Based on these facts, a major β was selected based on the following reasoning: i) a β for the
175 observation direction with lower (higher) γ_T for OH (PV) is selected. ii) in the case of OV (PH), for
176 which the rotating symmetric axis was observed for only one observation direction, β was considered
177 where the value of β had a higher (lower) γ_T than that of the other observation direction. Therefore, β
178 with a lower (higher) γ_T in two observation directions for the case of an oblate (prolate) particle was
179 considered as a meaningful value. The perfect sphere could not have their value of β determined
180 theoretically, because there is the possibility of a rotating symmetric axis in any direction.

181 Based on the definition of β (Fig. 2), the perfect condition with respect to ellipsoids is satisfied
182 when $|\beta| = 0^o$ (90^o) for OH and PV (OV and PH); these values are defined as the center values. However,
183 2DVD calculated that the β for each particle shape type was concentrated around $|\beta| = 0^o$ (90^o) with
184 respect to horizontally (vertically) oriented particles, which correspond to OH and PH (OV and PV).
185 Furthermore, analysis of particles with an orthogonal center angle from 0^o is difficult, since they have
186 two center angles ($\pm 90^o$). To address observation errors and enhance the convenience of analysis, all
187 center angles were set to $|\beta| = 0^o$ and modified to give the representative canting angle, β_R, using the
188 following equation:

189

190 $$\beta_R = \beta - \beta_0$$

191

where β_0 is the orienting angle, defined by the central angle of oscillation. In the case of vertically oriented particles (OV and PV), β_0 could be defined as $\pm 90^o$. The sign of β_0 follows that of β.

After removing β, each particle shape was defined using γ_T (Table 1). Note that a 10% bias range was allowed, to take observational error into account. For example, a particle was considered as a sphere when $0.9 < \gamma_T < 1.1$, which is an applied 10% bias range from $\gamma_T = 1$. In addition, the particle types OH and PV (OV and PH) were classified when the value of $|\gamma_1 - \gamma_2|$ was smaller (larger) than $0.1\gamma_T$, to consider particles with only a rotating symmetric axis.

c. Calculate the terminal velocity for the various particle shape types

The V_T of volcanic ash is required to estimate the R_A (kg m^{-2} s^{-1}) on the ground where this depends on atmospheric density (ρ_g in g cm^{-3}), T, Re, C_D, D, ρ_s, and its shape. Kunii and Levenspiel (1969) developed a theoretical V_T equation:

$$V_T = \left(\frac{4(\rho_s - \rho_g)gD}{3\rho_g C_D}\right)^{0.5} \qquad (10^0 < Re < 10^4)$$

Eq. (2)

Later, Suzuki (1983) developed a theoretical V_T equation for tephra. Bonadonna et al. (2011) then modified the theoretical V_T equation suggested by Kunii and Levenspiel (1969) with observed ash data, which implied that the result of the theoretical V_T equation could be unsuitable for non-spherical particles. Based on these equations, various C_D equations considering non-spherical particles were subsequently developed. Tran-Cong et al. (2004) developed a new equation for C_D using the function

of circularity and Hölzer and Sommerfeld (2008) introduced a progressed C_D equation considering two types of sphericity: lengthwise ($\Phi_{||}$) and crosswise ($\Phi_{\perp}$). This equation is as follows:

$$C_D = \frac{8}{Re}\frac{1}{\sqrt{\Phi_{||}}} + \frac{16}{Re}\frac{1}{\sqrt{\Phi}} + \frac{3}{\sqrt{Re}}\frac{1}{\Phi^{3/4}} + 0.42 \times 10^{0.41(-\log(\Phi))^{0.2}}\frac{1}{\Phi_{\perp}}$$

Eq. (3)

The Re is defined as:

$$Re = \frac{\rho_g V_T D}{\mu}$$

Eq. (4)

where μ is the dynamic viscosity (kg m^{-1} s^{-1}), which we assumed to be 1.983×10^{-5} based on atmospheric conditions at a T of 25 °C. Three types of sphericity were defined as follows:

$$\Phi = \frac{\pi D^2}{SA}$$

Eq. (5)

where SA is the surface area of the particle (mm^2). The lengthwise sphericity is defined as the ratio between the cross-sectional area of the volume-equivalent sphere and the difference between half the surface area and the mean of the projected vertical cross-sectional area (A_V) of the particle (Eq. 6):

$$\Phi_{||} = \frac{\pi D^2}{4(0.5 \times SA - A_V)}$$

Eq. (6)

The crosswise sphericity is the same as the lengthwise sphericity, except for the denominator, which includes the projected horizontal cross-sectional area of the particle (A_H), defined as follows:

$$\Phi_{\perp} = \frac{\pi D^2}{4A_H}$$

Eq. (7)

It is noteworthy that the V_T is required to calculate the Re and V_T, which refers to the final product. To solve this problem, the theoretical V_T (Eq. 2) was used as the input value of Eq. 4 until Eq. 2 converged.

d. Sakurajima volcano

Japan has around 10% (110) of all of the active volcanos in the world. Sakurajima (1,117m, 31.58º N, 130.65º E, Kyushu, Japan) is an active volcanic island formed around 13,000 years ago, and its tephra is approximately 60–66 % S_iO_2 Peléan-type (Oguchi et al., 2009; Takahashi et al., 2013). The major eruptive events in historic age of Sakurajima were 1471–1476 (Bunmei era), 1779–1782 (An-ei era) and 1914 (Taisho era). Sakurajima is an andesitic volcano with two peaks (Kita-dake and Minami-dake). Volcanic activity at Kita-dake ended around 4,900 years ago then it changed to Minami-dake. Activity has centred on Showa crater from 2006 (Iguchi, 2013). Showa crater is located on the eastern flank approximately 500 m east of Minami-dake (Southern Peak) of Sakurajima volcano. It was appeared in 1939 after one month of eruptions that year (Yokoo and Ishihara, 2007). The Minami-dake summit crater was the only active center of Sakurajima volcano until the recommencement of Showa

crater from 1948 to 2006. The eruptive activity of Showa crater was resumed in June 2006 and vulcanian eruptions gradually increased in the autumn of 2009 (Hotta et al., 2016). The Japan Meteorological Agency (JMA) reported that the eruption frequency of Sakurajima would increase significantly from 2009 and the accumulated ash fall exceeded 3.5 kg m^{-2} in Kagoshima city in 2012. The Ministry of Land, Infrastructure, Transport, and Tourism (MLITT) installed an operational X-band radar 10.7 km from the vent, as well as 16 automatic volcanic ash weight measurements, to observe volcanic eruptions in 2011 (Fig. 3).

e. Free fall experiments

The data were collected by automatic volcanic ash weight measurements performed on the Sakurajima volcano (Tajima et al., 2015; Maki et al., 2014; 2016). The free-fall experiments were divided into two types; one was performed for each phi scale ($\Phi = -\log_2 D$) from $\Phi = 3$ to -4 ($0.125 < D < 16$ mm), and the other was not considered on a particle size scale. The former data, expressed by A and B (Type 1), were collected at two sites and screened by size (Fig. 4); the latter data, expressed as C–E (Type 2), were collected at 18 sites (Table 2). Free-fall experiments on collected volcanic ash particles were carried out in the large-scale rainfall simulator of the National Research Institute for Earth Science and Disaster Prevention (NIED) in Tsukuba, Japan. The collected particles were dropped manually around 17 m from the ground and re-collected by a third-generation 2DVD (Maki et al., 2016). Each sample was dropped for 30 sec to stimulate dispersion, and the measurement period was 1 min. To avoid wind effects including turbulence, the 2DVD was surrounded by a 3^3 cubic meter windbreaking wall (Fig. 5).

The free-fall experiments were conducted at intervals of 1 min over 6 h 30 min, as shown in Fig. 6. The number of particles detected by 2DVD was less than 10,000 for 1 min, and the particle size

range of Type1 data set was proportional to its phi-scale, since small particles may be contained by screening.

Figure 7 shows the distribution of raw data (the number of data: 274,215) for V_T and γ with D. There were various γ from 0 to 2 when $D < 2$ mm and most of the data were concentrated near $\gamma = 0$. The γ values converged around 1 and their distributional range decreased with D. The median value with a 0.25 mm D interval corresponded well to the center of the data contour. The median line converged around $\gamma = 0.935$ based on the correlation coefficient value (CC). When this was higher than 0.95 for each D interval, the data converged. According to this condition, the range of $2 < D < 5$ mm was satisfied and the mean value was calculated using these data. The V_T had a wider range when $D < 2$ mm but the median line corresponded well to the center of the data (Fig. 7b). The line representing the largest amount of data is lower than the volcanic ash discussed by Bonadonna et al. (2011). To select a available range of D, a theoretical terminal velocity equation ($V_{T,Ref}$) for a non-sphere corresponding to Eqs. 2–7 was used as the reference. The particle density associated with the eruption of Sakurajima volcano is between 2.43 and 2.59 g cm^{-3} (Oguchi et al., 2009), but the actual particles contain air vacuoles (Van Eaton et al., 2012). This means that ρ_s, including vacuoles, is smaller than ρ_s. Therefore, the minimum ρ_s was considered to be 2.43 g cm^{-3}, and this was used as an input parameter. The atmospheric conditions of T and P were considered from an automatic weather station (AWS), supported by the JMA. The falling height of a particle which follows the aforementioned conditions ($\gamma = 0.935$, $\rho_s = 2.43$ g cm^{-3}) when $D = 4$ was lower than that under the condition of free fall experiment (17 m) when it reached 90% of V_T (13.9 m); therefore, the available data range is considered to be $D \leq 4$ mm, and this would satisfy the terminal fall velocity. The detailed equations used in the present study are shown in Appendix A.

f. Quality control procedures

The 2DVD was originally developed to detect raindrop hydrometeors. For this reason, additional quality control (QC) checks were deemed necessary to ensure applicability to non-hydrometeors, such as volcanic ash particles. Specifically, we performed the following three QC procedures for accurate analysis of the data:

i) Particle $D > 0.25$ mm was selected in consideration of the minimum spatial resolution of 2DVD.

ii) If the major axis observed by 2DVD was 10% longer than that of the value calculated directly based on data coordinates, the data were considered erroneous and thus removed. A 10% bias range was considered due to mathematical error, the irregular particle shape, and the limitation of the spatiotemporal resolution of 2DVD.

iii) To consider volcanic ash particle, the sample satisfying in the certain range of terminal velocity relationship was selected. If we consider a single V_T QC measure for the entire particle shape types, a number of available data will be removed since V_T critically depends on particle shape. Therefore, we applied a 60% V_T QC threshold (Jaffrain et al., 2011) for each particle shape type. It could be applied once V_T relationship of volcanic ash particles is obtained. After selecting the particle shape types and applying these two QC procedures (i and ii), 19.31% of the data (62,953) remained (Table 1).

3. Results

a. Ash particle shape

The ash particle size over the entire volcanic ash sample was skewed leftward, and the dominant particle shape type changed with particle size (Fig. 8). The particles were predominantly horizontally oriented (75.51%) and vertically oriented (21.60%). Oblate and prolate spheroids made up 76.26% and 23.85% of the particles, respectively. Hence, the particles were mainly OH (57.38%) or PH (15.88%) (Table 2). The particles were predominantly $0.25 < D < 0.5$ mm (63.00%) or $0.5 < D < 1$ mm (32.80%). Relatively few particles had $D > 1$ mm (4.20%).

There was large variation in shape among particles $0.25 < D < 0.5$ mm, but the variation decreased with increasing D. All of the particle shape types had the largest number of particle at $D > 1.0$ mm and the next were shown at $0.5 < D < 1.0$ mm, except for OH. In total, 95.80% of OH particles had $D < 1$ mm; at $D < 0.5$ mm, the value was 75.68%, and at D = 0.5–1 mm, it was 22.36%. In the cases of PH and OV, 93.63% and 93.87% of these particles, respectively, had $D < 1$ mm. Beyond $D > 1$ mm, the differences in the number of particles for each particle shape type were considerably decreased.

b. Terminal velocity

The V_T for the entire particle shape types well follows a polynomial regression analysis which was applied to define the nonlinear relationship between V_T and D (Fig. 9a). It corresponds to that obtained by Miwa et al (2015), who analyzed Parsivel data using the same laboratory experiments. There was the inflection point of V_T at $D < 1.3$ mm and it came from an increase in the number of OH and an decrease in their V_T when $D < 1$ mm. It can be seen the V_T relationship for each particle shape type.

The observed values of V_T were well classified by particle shapes (Fig. 9b). The highest values of V_T were recorded in the order of prolate, sphere, and oblate. Vertically oriented particles had higher V_T values than horizontal ones. The V_T for every particle type can be expressed in a power-law form, except for OH. OH particles followed the regression line relatively closely, and showed the highest CC and root mean square error (RMSE) values, of 0.94 and 0.46 m s^{-1}, respectively. Horizontally orientated particles had relatively higher correlations (OH: 0.94, PH: 0.87) compared to those with a vertical orientation (OV: 0.75, PV: 0.71). The V_T relationships and those of statistical parameters are summarized in Table 3.

To verify the reliability of the particle data obtained by 2DVD, which was originally developed to detect liquid raindrops, ρ_s, C_D, and Re, as well as theoretical V_T values according to these parameters, were analyzed. To calculate the parameters of interest, including the surface area and cross-sectional area of irregular particles, we applied the irregular particle volume estimation equations of Huang et al. (2010).

c. Aerodynamic properties

Particle densities were estimated using the $V_{T,Ref}$, converged to 2.37 g cm^{-3} when D < 1.5 mm (Fig. 10a). This value corresponds well to that of the minimum ρ_s (2.43 g cm^{-3}) reported by Oguchi et al. (2009). The slight difference is likely due to observation errors and the presence of vesicles (e.g., Seligman et al., 2016). The median value of ρ_s is changed to 0.5 < D < 1.5 mm, and this range corresponds to that of V_T. Horizontally oriented particles (OH and PH) have relatively smaller ρ_s and vertically oriented particles (OV and PV) have higher density (Fig. 10b); spheres have particle densities that accord best with D. The median ρ_s values for all particle shapes converged when D < 2 mm, and the converged ρ_s values ranged from 2.35 to 2.50 g cm^{-3}.

375 The Re and C_D for the all particle shapes ranged from 10 to 4,000 and 0.6 to 20, respectively (Fig.
376 11a). Higher values of C_D were observed when log(Re) < 1.845 (Re < 70); above this threshold, C_D
377 dramatically decreased. These results were derived according to the number of OH particles, which
378 mainly had D < 0.5 mm, and had higher C_D and lower Re. Particle shape was divided into two types:
379 OH and others (Fig. 11b). OH particles had higher C_D compared to the other particle shapes, which in
380 turn showed few differences among themselves. The OH particles experience strong drag forces under
381 the same flow conditions, leading to lower V_T. The differences between OH and other particles
382 diminished with Re < 1,000. The other particle shapes had relatively higher C_D in the range 10 < Re <
383 3,000. Rong et al. (2015) analyzed the relationship between Re and C_D for oblate and prolate particles,
384 and showed that OH particles had higher C_D compared to the reference line (Clift and Gauven, 1971)
385 in the range 0 < Re < 400. Each relationship is summarized in Fig. 11.
386
387
388 **d. Axis ratio**
389 The γ of a particle affects the backscattering power of electromagnetic waves, and it is necessary
390 to calculate the horizontal reflectivity (Z in dBZ), differential reflectivity (Z_{DR} in dB), and specific
391 differential phase shift (K_{DP} in ° km^{-1}). Note that previous studies have analyzed the γ distribution for
392 raindrops and snow, including hail; however, few studies have been reported on γ of ash particles
393 compared to those for hydrometeor.
394 Figure 12 shows the quartiles and median values of γ for the entire particle shapes, and for each
395 individual particle shape type. The γ had a higher standard deviation (σ_γ) of > 0.25 when D < 0.75 mm,
396 which decreased and converged to σ_γ = 0.15 when D > 1 mm (Fig. 12a). The γ in the lower σ_γ range
397 converged to γ = 0.94 and could be expressed as follows:
398

$$\gamma(\mathrm{D}) = 0.94 - 0.25\exp(-1.90\ \mathrm{D})$$

Eq. (8)

The particles are more easily classified by shape than by V_T (Fig. 12b). Every particle shape type was independent of D, except for OH. The γ of each particle types are expressed the following relationships (Eqs. 9–12):

$$\gamma(\mathrm{D})_{OH} = 0.37\tanh(1.84\mathrm{D} - 1.88) + 0.38$$

Eq. (9)

$$\gamma_{OV} = 1.15$$

Eq. (10)

$$\gamma_{PH} = 0.88$$

Eq. (11)

$$\gamma_{PV} = 1.24$$

Eq. (12)

The parameter $\gamma(\mathrm{D})_{OH}$ was calculated using the hyperbolic tangent (tanh) for the following reasons: i) its range of values was wider than those of other particle types; ii) the data distribution changed continuously with D; and iii) it was present in a higher proportion (30.44%) compared to the other parameters. We found that variations in γ decreased with D and the proportion of Sp shapes increased when D > 2 mm. The particle types OV and PH showed a wide distribution over $1 < \gamma < 1.5$ and $0.4 < \gamma < 1.0$, respectively, when D < 2 mm, but the variability in median values was relatively low. The relationships of γ for each particle shape type could be expressed by constant values at γ = 0.75 (OH), 0.88 (PH), 1.15 (OV), and 1.24 (PV), respectively, and these differences are around γ = 0.12.

e. Canting angle

Statistical analysis of β is required to understand the aerodynamic properties of volcanic ash particles, and the input parameters of T-matrix scattering simulations, to verify the observed radar variables. The histogram of β_R can be shown in Fig. 13

More than 95% of β values for each particle shape type were concentrated in the range $|\beta_R| \leq 30^o$, with 0^o as the center (Fig. 13). The particles were symmetrically distributed around 0^o and more than 50% were concentrated in the range $|\beta_R| < 4^o$. The horizontally oriented β distribution was relatively narrow ($|\beta_R| < 20^o$) and exhibited a unimodal distribution. It is noteworthy that 90% of OH particles were concentrated in the range $|\beta_R| < 4^o$. The vertically oriented β distribution was relatively broader ($|\beta_R| < 30^o$) and followed a bimodal distribution. PV exhibited a bimodal form, but this was not symmetrical about 0^o. For spheres, the β distribution was narrower, similar to horizontally oriented particles, and it had a bimodal distribution, similar to vertically oriented particles, indicating that the independent features of both orientations were combined.

The values of $|\overline{\beta_R}|$ and $|\sigma_\beta|$ for OH and PV (OV, PH) were 0^o and 3.5^o (0.4^o, 13.1^o), and 1.3^o and 12.7^o (0.2^o, 10.9^o), respectively. OV (OH) had the highest (lowest) value of $|\sigma_\beta|$. This validates the assumption of Marzano et al. (2012) under stable conditions ($|\sigma_\beta| = 10°$). Therefore, we believe that the tumbling phenomenon ($|\sigma_\beta| > 30°$) of the particles under calm atmospheric conditions was likely to be minor.

To analyze the correlation between particle D and β, quartiles for each particle D interval were calculated (Fig. 14). The particles were concentrated at $|\beta_R| < 30°$ regardless of D, and median values were stable when D < 1 mm for the entire particle shape types; however, fluctuation increased with D (Fig. 14a). The $|\sigma_\beta|$ values gradually increased from 10° to 13° when 0.3 < D < 1.3 mm and variability was greatest around the center (13°). This increase in $|\sigma_\beta|$ would not be expected in the case of a

447 relatively small number of particles (Fig. 8a), since their standard deviation is largely maintained at
448 about 13° regardless of dataset size.

449 Variability in the median values for individual particles was more apparent. The values converged
450 around 0° but fluctuation increased with greater D from the zero line. The median $|\beta_R|$ values
451 exceeded 3°, 5°, 10°, and 15° when $D > 1$ mm, $1 < D < 2$ mm, $2 < D < 3$ mm, and $D > 3$ mm,
452 respectively (Fig. 14b).

453

4. Discussions

The results of present study can be extended in viewpoint of the radar meteorology: i) the radar observation and ii) ashfall rate (R_A) estimations. i) Weather radar operates for a similar purpose to that of meteorological satellites, and provides information for determining the volume, mass, and echo top height of weather systems. Short-duration eruptions, i.e., less than 1 hour, can be detected at high spatio-temporal resolution, especially in the early period of an eruption. The temporal resolution of weather radar is a few minutes for a single volume scan, and depends on the observation strategy and radar band. The spatial resolution of weather radar is a few hundred meters and is proportional to the radar frequency. A number of ash cloud detections were reported in several observational cases in the US and Japan (Maki and Doviak, 2001; Maki et al., 2012). Marzano et al. (2013) summarized 28 major explosive volcanic eruptions detected by weather radars from 1970 to 2011. Harris and Rose (1983) attempted to analyze volcanic ash particle size and total mass using a C-band weather radar. Maki and Doviak (2001) proposed the method to retrieve PSD from radar measurements of volcanic ash and Donnadieu et al. (2012) detected volcanic eruptions using an L-band fixed radar. Marzano et al. (2006, 2012) and Maki et al. (2012, 2014) detected and analyzed volcanic eruptions using weather radars, from theoretical (physical) and experimental (engineering) perspectives. Thus, observability of volcanic ash clouds using weather radar can be confirmed from previous researches. To verify radar-based volcanic ash cloud observations, a scattering simulation can be considered. The basic parameters: axis ratio, canting angle which are the results presented in this study are the input information of scattering simulation to simulate the theoretical radar variables. In particular, the T-matrix scattering simulation developed by Waterman (1965) is useful for calculation of the theoretical backscattering power of non-spherical particles.

Seconds, the V_T is one of the main parameters for R_A (kg m^{-2} hr^{-1}) and it is defined in terms of PSD and V_T as follows:

478

479 $$R_A = V_r \frac{3.6}{10^3} \int_{D_1}^{D_2} V_T(D) N(D) D^3 dD$$

480 Eq. (13)

481

482 where V_r is the particle volume ratio. In case of sphere, it is considered as $\pi/6$.

483 Marzano et al. (2012b) proposed Z-C_A relationships using the ashfall concentration (C_A in g m^{-3})
484 and z. Maki et al. (2016) introduced R_A-z relationship for Sakurajima eruption case (18. Aug. 2013)
485 using the time integration of R_A (S_A in kg m^{-2}) obtained by automatic volcanic ash weight
486 measurements. However, once we use the disdrometer such as 2DVD, it will be possible to estimate
487 R_A directly since 2DVD can measure PSD, V_T and γ. Therefore, basic parameters could help to
488 simulate radar variables and estimate R_A which are necessary to develop the quantitative ash fall
489 estimation (QAE) method.

490

5. Summary and Conclusions

The basic parameters (V_T, γ and β) of volcanic ash particles were analyzed from the free fall experiments with 2DVD. Data were collected with 18 automatic volcanic ash weight measurements performed on Sakurajima volcano, Japan (31.58º N, 130.65º E). To identify the aerodynamic properties of the volcanic ash particles in the samples, a free-fall experiment was conducted in the large-scale rainfall simulator of the NIED, and 274,215 samples were analyzed.

Radar variables are highly dependent on the $|K|^2$, size, and shape of particles. Particle types with rotating symmetric axes were assumed to represent volcanic ash particles which have a wide variety of irregular shape. Their orientation was also considered with respect to horizontally (OH, PH) and vertically (OV, PV) oriented oblate and prolate spheroids were studied, respectively.

The dominant particle shape comprised horizontally and vertical oriented particles, present in proportions of 75.51% and 21.60%, respectively. Regarding particle shape, oblate (prolate) spheroids comprised 76.26% (23.85%) of all particles in the samples. The most common particle shape type was OH, accounting for 59% of all particles when $D < 1$ mm, and 69% when $D < 0.5$ mm. Overall, 95.80%, 93.87%, and 93.63% of the OH, OV, and PH particles had $D < 1$ mm, respectively.

The V_T of the particles were classified in the order of PV, OV, Sp, PH and OH. These results are consistent with the $V_{T, Ref}$, which suggests that 2DVD is a reliable for observing volcanic ash particles under stable weather conditions. A noticeable increase in V_T for OH in the range $0.5 < D < 1$ mm occurred through an increase in γ; this was not observed for other particle types.

The estimated ρ_s converged to 2.37g cm^{-3} when $D > 1.5$ mm, and the median value changed over the range $0.5 < D < 1.5$ mm. The converged value of ρ_s is consistent with the value for the Sakurajima volcano reported by Oguchi et al. (2009). The relationship of C_D and Re were divided into two particle type categories (OH and the others) and C_D(OH) was dramatically increased in the range of $Re < 70$. These results were derived from the particle concentration of OH, which was highest when $D < 0.5$

515 mm; at this threshold, C_D was higher and Re was lower. The range of V_T over $0.7 < D < 1.3$ mm was
516 informed by both γ and ρ_s.

517 The σ_γ decreased in the range of $D > 0.75$ mm, to 0.15, and converged to $\gamma = 0.94$. Maki et al.
518 (2014) introduced the radar variables and found that Z_{DR} gradually increased with time; the dominant
519 values at 10 and 18 min after the eruption were close to 1 and 2 dB, respectively. The results presented
520 in this study corresponded to volcanic eruption clouds with positive Z_{DR} since it is a function of $|K|^2$
521 and γ (Herzegh and Jameson, 1992). In addition, it can be explained that the size sorting of ash particle
522 (e.g., Beckett et al., 2015; Stevenson et al., 2015) will affect the increase of ZDR by the results of
523 present study.

524 The $|\sigma_\beta|$ of OV particles with $|\beta_0| = 90^\circ$ was largest (13.1˚) among all particle types and OH particles
525 had the lowest $|\sigma_\beta|$ at 3.5˚. Based on the $|\sigma_\beta|$ results, the tumbling phenomenon would not be dominant
526 under calm atmospheric conditions. The quartiles were stable when $D < 1$ mm for the entire particle
527 shape types, but increased with D. The value of σ_β was higher when $D < 1.3$ mm and started to converge
528 around 13°due to a decrease in the number of OH particles.

529 These results could be the essential information to develop the new approaches for detecting non-
530 hydrometeors and numerical model. The axis ratio and canting angle of ash particles obtained from
531 the present study are necessary for scattering simulations. V_T obtained by the present study suggests
532 that smaller particles can be transported longer distance. Therefore, it will be useful for scattering
533 simulation of ash particles to develop QAE and help to improve a numerical model using V_T obtained
534 by the present study.

535

Author contributions

Masato Iguchi and Masayuki Maki designed the study. Akihiko Yamaji and Tatsuya Momotani collected the samples and performed the free-fall experiment. Sung-Ho Suh modified the original study theme and performed the study. Masayuki Maki and Sung-Ho Suh performed research, obtained the results and prepared the manuscript along with contributions from all of the co-authors. Dong-In Lee examined the results and checked the manuscript.

Acknowledgments

This work was supported by a Grant-in Aid for JSPS KAKENHI (grant number JP16H03145) and partially supported by a DPRI collaborative research grant (Kyoto Univ. 25G-11). The authors acknowledge the provision of ashfall data and funding for this work from Kyoto and Kagoshima Universities. The 2DVD data were provided by MEXT, Japan. We also thank the NIED for use of their large-rainfall simulator.

Appendix A

The theoretical fall velocity and falling distance with time are calculated as follows;

$$F = ma = F_g - F_D \quad \text{Eq. (A1)}$$

$$F_g = mg \quad \text{Eq. (A2)}$$

$$F_D = \frac{1}{2}\rho_g V^2 C_D A \quad \text{Eq. (A3)}$$

where F_g is universal gravitation, F_D is drag force, m is mass, and a is the free-fall acceleration. In Eq. A2, g is the acceleration due to gravity, considered to be 9.81 m s^{-2}, and V and C_D in Eq. A3 correspond to the values in Eq. 2–7. The symbols μ and ρ_g are the dynamic viscosity and density of the atmosphere and were assumed as 1.837×10^{-5} kg m^{-1} s^{-1} and 1.194×10^{-5} g cm^{-3}, respectively. The results were based on conditions at an atmospheric T as 25 °C.

To ensure accuracy, we considered the surface roughness effect of a volcanic ash particle (1.07^{-1}) on the fall velocity, as suggested by Bagheri and Bonadonna (2016), and the results for D = 4 mm are shown in Fig. A1.

569 # References

570 Böhm, H. P.: A general equation for the terminal fall speed of solid hydrometeors, Journal of the
571 Atmospheric Sciences, 46, 2419-2427, 1989.

572 Bagheri, G., Bonadonna, C., Manzella, I., Pontelandolfo, P., and Haas, P.: Dedicated vertical wind
573 tunnel for the study of sedimentation of non-spherical particles, Review of Scientific
574 Instruments, 84, 054501, 2013.

575 Bagheri, G. and Bonadonna, C.: On the drag of freely falling non-spherical particles, Powder
576 Technology, 301, 526-544, 2016.

577 Beckett, F., Witham, C., Hort, M., Stevenson, J., Bonadonna, C., and Millington, S.: Sensitivity of
578 dispersion model forecasts of volcanic ash clouds to the physical characteristics of the
579 particles, Journal of Geophysical Research: Atmospheres, 120, 2015.

580 Bonadonna, C., Ernst, G., and Sparks, R.: Thickness variations and volume estimates of tephra fall
581 deposits: the importance of particle Reynolds number, Journal of Volcanology and
582 Geothermal Research, 81, 173-187, 1998.

583 Bonadonna, C., Genco, R., Gouhier, M., Pistolesi, M., Cioni, R., Alfano, F., Hoskuldsson, A., and
584 Ripepe, M.: Tephra sedimentation during the 2010 Eyjafjallajökull eruption (Iceland)
585 from deposit, radar, and satellite observations, Journal of Geophysical Research: Solid
586 Earth (1978–2012), 116, 2011.

587 Bonadonna, C., Folch, A., Loughlin, S., and Puempel, H.: Future developments in modelling and
588 monitoring of volcanic ash clouds: outcomes from the first IAVCEI-WMO workshop on
589 Ash Dispersal Forecast and Civil Aviation, Bulletin of volcanology, 74, 1-10, 2012.

590 Clift, R. and Gauvin, W.: Motion of particles in turbulent gas streams, British Chemical Engineering,
591 16, 229-&, 1971.

592 Coltelli, M., Miraglia, L., and Scollo, S.: Characterization of shape and terminal velocity of tephra
593 particles erupted during the 2002 eruption of Etna volcano, Italy, Bulletin of volcanology,
594 70, 1103-1112, 2008.

595 Del Bello, E., Taddeucci, J., Vitturi, M. d. M., Scarlato, P., Andronico, D., Scollo, S., Kueppers, U.,
596 and Ricci, T.: Effect of particle volume fraction on the settling velocity of volcanic ash
597 particles: insights from joint experimental and numerical simulations, Scientific reports,
598 7, 39620, 2017.

599 Dellino, P., Mele, D., Bonasia, R., Braia, G., La Volpe, L., and Sulpizio, R.: The analysis of the
600 influence of pumice shape on its terminal velocity, Geophysical Research Letters, 32,
601 2005.

602 Dioguardi, F., Mele, D., Dellino, P., and Dürig, T.: The terminal velocity of volcanic particles with
603 shape obtained from 3D X-ray microtomography, Journal of Volcanology and Geothermal
604 Research, 329, 41-53, 2017.

605 Dioguardi, F., Mele, D., and Dellino, P.: A New One-Equation Model of Fluid Drag for Irregularly
606 Shaped Particles Valid Over a Wide Range of Reynolds Number, Journal of Geophysical
607 Research: Solid Earth, 123, 144-156, 2018.

608 Donnadieu, F.: Volcanological applications of Doppler radars: A review and examples from a
609 transportable pulse radar in L-band, INTECH Open Access Publisher, 2012.

610 Folch, A., Costa, A., and Macedonio, G.: FALL3D: A computational model for transport and
611 deposition of volcanic ash, Computers & Geosciences, 35, 1334-1342, 2009.

612 Ganser, G. H.: A rational approach to drag prediction of spherical and nonspherical particles, Powder
613 Technology, 77, 143-152, 1993.

614 Garboczi, E. and Bullard, J.: 3D analytical mathematical models of random star-shape particles via a
615 combination of X-ray computed microtomography and spherical harmonic analysis,
616 Advanced Powder Technology, 28, 325-339, 2017.

617 Hölzer, A. and Sommerfeld, M.: New simple correlation formula for the drag coefficient of non-
618 spherical particles, Powder Technology, 184, 361-365, 2008.

619 Haider, A. and Levenspiel, O.: Drag coefficient and terminal velocity of spherical and nonspherical
620 particles, Powder technology, 58, 63-70, 1989.

621 Happel, J. and Brenner, H.: Low Reynolds number hydrodynamics: with special applications to
622 particulate media, Springer Science & Business Media, 2012.

623 Harris, D. M. and Rose, W. I.: Estimating particle sizes, concentrations, and total mass of ash in
624 volcanic clouds using weather radar, Journal of Geophysical Research: Oceans (1978–
625 2012), 88, 10969-10983, 1983.

626 Herzegh, P. H. and Jameson, A. R.: Observing precipitation through dual-polarization radar
627 measurements, Bulletin of the American Meteorological Society, 73, 1365-1376, 1992.

628 Hotta, K., Iguchi, M., and Tameguri, T.: Rapid dike intrusion into Sakurajima volcano on August 15,
629 2015, as detected by multi-parameter ground deformation observations, Earth, Planets and
630 Space, 68, 68, 2016.

631 Huang, G.-J., Bringi, V., Cifelli, R., Hudak, D., and Petersen, W.: A methodology to derive radar
632 reflectivity-liquid equivalent snow rate relations using C-band radar and a 2D video
633 disdrometer, Journal of Atmospheric and Oceanic Technology, 27, 637-651, 2010.

Huang, G.-J., Bringi, V., Moisseev, D., Petersen, W. A., Bliven, L., and Hudak, D.: Use of 2D-video disdrometer to derive mean density–size and Z e–SR relations: Four snow cases from the light precipitation validation experiment, Atmospheric Research, 153, 34-48, 2015.

Iguchi, M.: Magma Movement from the Deep to Shallow Sakurajima Volcano as Revealed by Geophysical Observations (< Special Section> Sakurajima Special Issue), Bulletin of the Volcanological Society of Japan, 58, 1-18, 2013.

Jaffrain, J., Studzinski, A., and Berne, A.: A network of disdrometers to quantify the small-scale variability of the raindrop size distribution, Water Resources Research, 47, 2011.

Joss, J., and Waldvogel A.: A spectrograph for the automatic analysis of raindrops, Pure and Applied Geophysics, 69, 240-246, 1967.

Kruger, A. and Krajewski, W. F.: Two-dimensional video disdrometer: A description, Journal of Atmospheric and Oceanic Technology, 19, 602-617, 2002.

Kunii, D.: 0. Levenspiel, Fluidization Engineering, John Wiley, 8, 44-45, 1969.

Langmann, B., Folch, A., Hensch, M., and Matthias, V.: Volcanic ash over Europe during the eruption of Eyjafjallajökull on Iceland, April–May 2010, Atmospheric Environment, 48, 1-8, 2012.

Löffler-Mang, M. and Joss. J: An optical disdrometer for measuring size and velocity of hydrometeors, Journal of Atmospheric and Oceanic Technology, 17, 130-139, 2000.

Maki, M. and Doviak, R.: Volcanic ash size distribution determined by weather radar, 1810-1811, 2001.

Maki, M., Maesaka, T., Kozono, T., Nagai, M., Furukawa, R., Nakada, S., Koshida, T., and Takenaka, H.: Quantitative volcanic ash estimation by operational polarimetric weather radar, 2012.

Maki, M., Maesaka, T., Muraji, Y., and Suzuki, I.: Statistical analysis of volcanic ash measured by X-band polarimetric radar, 2014.

Maki, M., Iguchi, M., Maesaka, T., Miwa, T., Tanada, T., Kozono, T., Momotani, T., Yamaji, A., and Kakimoto, I.: Preliminary results of weather radar observations of sakurajima volcanic smoke, Journal of Disaster Research, 11, 15-30, 2016.

Marzano, F. S., Barbieri, S., Vulpiani, G., and Rose, W. I.: Volcanic ash cloud retrieval by ground-based microwave weather radar, IEEE transactions on geoscience and remote sensing, 44, 3235-3246, 2006.

Marzano, F. S., Picciotti, E., Vulpiani, G., and Montopoli, M.: Synthetic signatures of volcanic ash cloud particles from X-band dual-polarization radar, IEEE Transactions on Geoscience and Remote Sensing, 50, 193-211, 2012.

Marzano, F. S., Picciotti, E., Montopoli, M., and Vulpiani, G.: Inside volcanic clouds: Remote sensing of ash plumes using microwave weather radars, Bulletin of the American Meteorological Society, 94, 1567-1586, 2013.

Nešpor, V., Krajewski, W. F., and Kruger, A.: Wind-induced error of raindrop size distribution measurement using a two-dimensional video disdrometer, Journal of Atmospheric and Oceanic Technology, 17, 1483-1492, 2000.

Oguchi, T., Udagawa, M., Nanba, N., Maki, M., and Ishimine, Y.: Measurements of dielectric constant of volcanic ash erupted from five volcanoes in Japan, IEEE Transactions on Geoscience and Remote Sensing, 47, 1089-1096, 2009.

675 Poulidis, A. P., Takemi, T., Iguchi, M., and Renfrew, I. A.: Orographic effects on the transport and
676 deposition of volcanic ash: A case study of Mount Sakurajima, Japan, Journal of
677 Geophysical Research: Atmospheres, 122, 9332-9350, 2017.

678 Rong, L., Zhou, Z., and Yu, A.: Lattice–Boltzmann simulation of fluid flow through packed beds of
679 uniform ellipsoids, Powder Technology, 285, 146-156, 2015.

680 Rosenfeld, D. and Ulbrich, C. W.: Cloud microphysical properties, processes, and rainfall estimation
681 opportunities. In: Radar and Atmospheric Science: A Collection of Essays in Honor of
682 David Atlas, Springer, 2003.

683 Seligman, A. N., Bindeman, I. N., Watkins, J. M., and Ross, A. M.: Water in volcanic glass: From
684 volcanic degassing to secondary hydration, Geochimica et Cosmochimica Acta, 191, 216-
685 238, 2016.

686 Sheppard, B. E.: Measurement of raindrop size distributions using a small Doppler radar, Journal of
687 Atmospheric and Oceanic Technology, 7, 255-268, 1990.

688 Sigurdsson, H., Houghton, B., McNutt, S., Rymer, H., and Stix, J.: The encyclopedia of volcanoes,
689 Elsevier, 2015.

690 Stevenson, J., Millington, S., Beckett, F., Swindles, G., and Thordarson, T.: Big grains go far:
691 understanding the discrepancy between tephrochronology and satellite infrared
692 measurements of volcanic ash, Atmospheric Measurement Techniques, 8, 2069-2091,
693 2015.

694 Stokes, G. G.: On the effect of the internal friction of fluids on the motion of pendulums, Pitt Press
695 Cambridge, 1851.

696 Suzuki, T.: A theoretical model for dispersion of tephra, Arc volcanism: physics and tectonics, 95, 113,
697 1983.

698 Takahashi, M., Otsuka, T., Sako, H., Kawamata, H., Yasui, M., Kanamaru, T., Otsuki, M., Kobayashi,
699 T., Ishihara, K., and Miki, D.: Temporal Variation for Magmatic Chemistry of the
700 Sakurajima Volcano and Aira Caldera Region, Southern Kyushu, Southwest Japan since
701 61 ka and Its Implications for the Evolution of Magma Chamber System, Bulletin of the
702 Volcanological Society of Japan, 58, 19-42, 2013.

703 Tajima, Y., Ohara, D., Fukuda, K., and Shimomura, S.: Development of Automatic Tephrometer for
704 Monitoring of Volcano, 39-46, 2015.

705 Thurai, M. and Bringi, V.: Drop axis ratios from a 2D video disdrometer, Journal of Atmospheric and
706 Oceanic Technology, 22, 966-978, 2005.

707 Tokay, A., Wolff, D. B., and Petersen, W. A.: Evaluation of the new version of the laser-optical
708 disdrometer, OTT Parsivel2, Journal of Atmospheric and Oceanic Technology, 31, 1276-
709 1288, 2014.

710 Tran-Cong, S., Gay, M., and Michaelides, E. E.: Drag coefficients of irregularly shaped particles,
711 Powder Technology, 139, 21-32, 2004.

712 Van Eaton, A. R., Muirhead, J. D., Wilson, C. J., and Cimarelli, C.: Growth of volcanic ash aggregates
713 in the presence of liquid water and ice: an experimental approach, Bulletin of volcanology,
714 74, 1963-1984, 2012.

715 Waterman, P. C.: Symmetry, unitarity, and geometry in electromagnetic scattering, Physical review D,
716 3, 825, 1971.

717 Wilson, L. and Huang, T.: The influence of shape on the atmospheric settling velocity of volcanic ash
718 particles, Earth and Planetary Science Letters, 44, 311-324, 1979.

719 Wilson, T. M., Stewart, C., Sword-Daniels, V., Leonard, G. S., Johnston, D. M., Cole, J. W., Wardman,
720 J., Wilson, G., and Barnard, S. T.: Volcanic ash impacts on critical infrastructure, Physics
721 and Chemistry of the Earth, Parts A/B/C, 45, 5-23, 2012.

722 Wilson, T. M., Jenkins, S., and Stewart, C.: Impacts from volcanic ash fall. In: Volcanic Hazards,
723 Risks and Disasters, Elsevier, 2015.

724 Yokoo, A. and Ishihara, K.: Volcanic activity around Showa Crater of Sakurajima Volcano monitored
725 with infrared and video cameras, Annuals of Disas. Prev. Res. Inst., Kyoto Univ., No. 50
726 C., 2007.

727

728

Figures

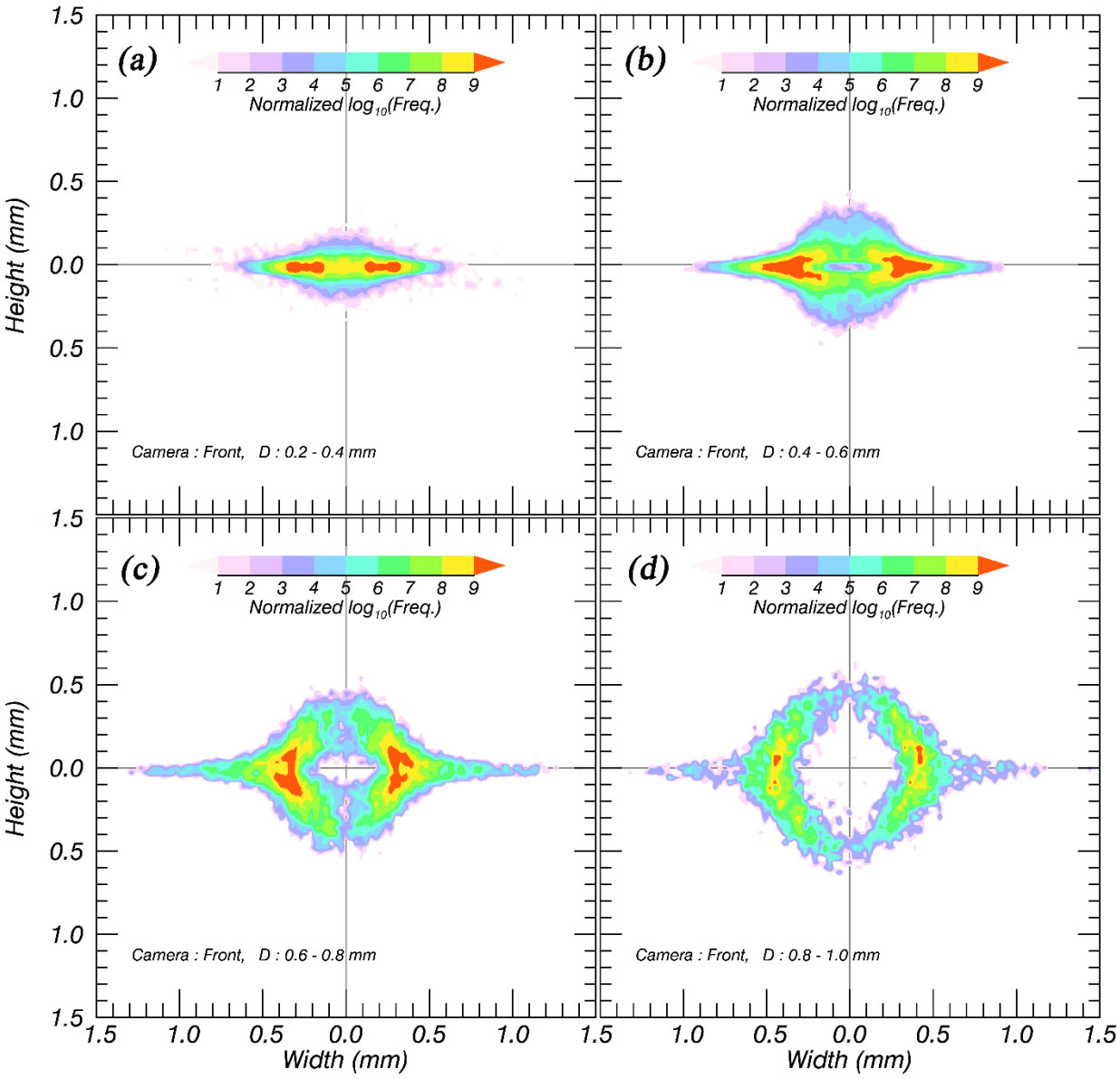

Figure 1. Accumulated contoured images of volcanic ash particles with D measured by a two-dimensional video disdrometer (2DVD).

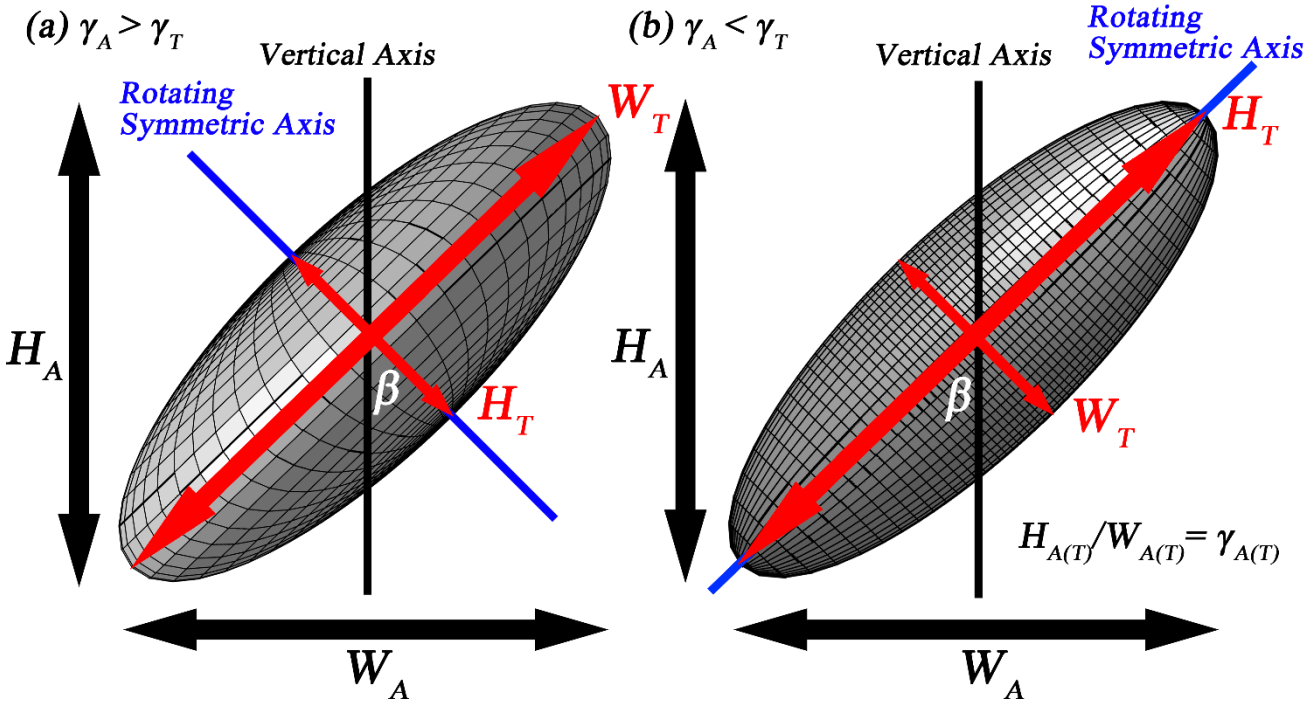

737

738 Figure 2. Conceptual model of an (a) oblate and (b) prolate spheroid with the same canting angle
739 (β). $W_{A(T)}$ and $H_{A(T)}$ are the apparent (true) width and height of the particle, respectively. $\gamma_{A(T)}$ is the
740 apparent (true) axis ratio.

741

742

743

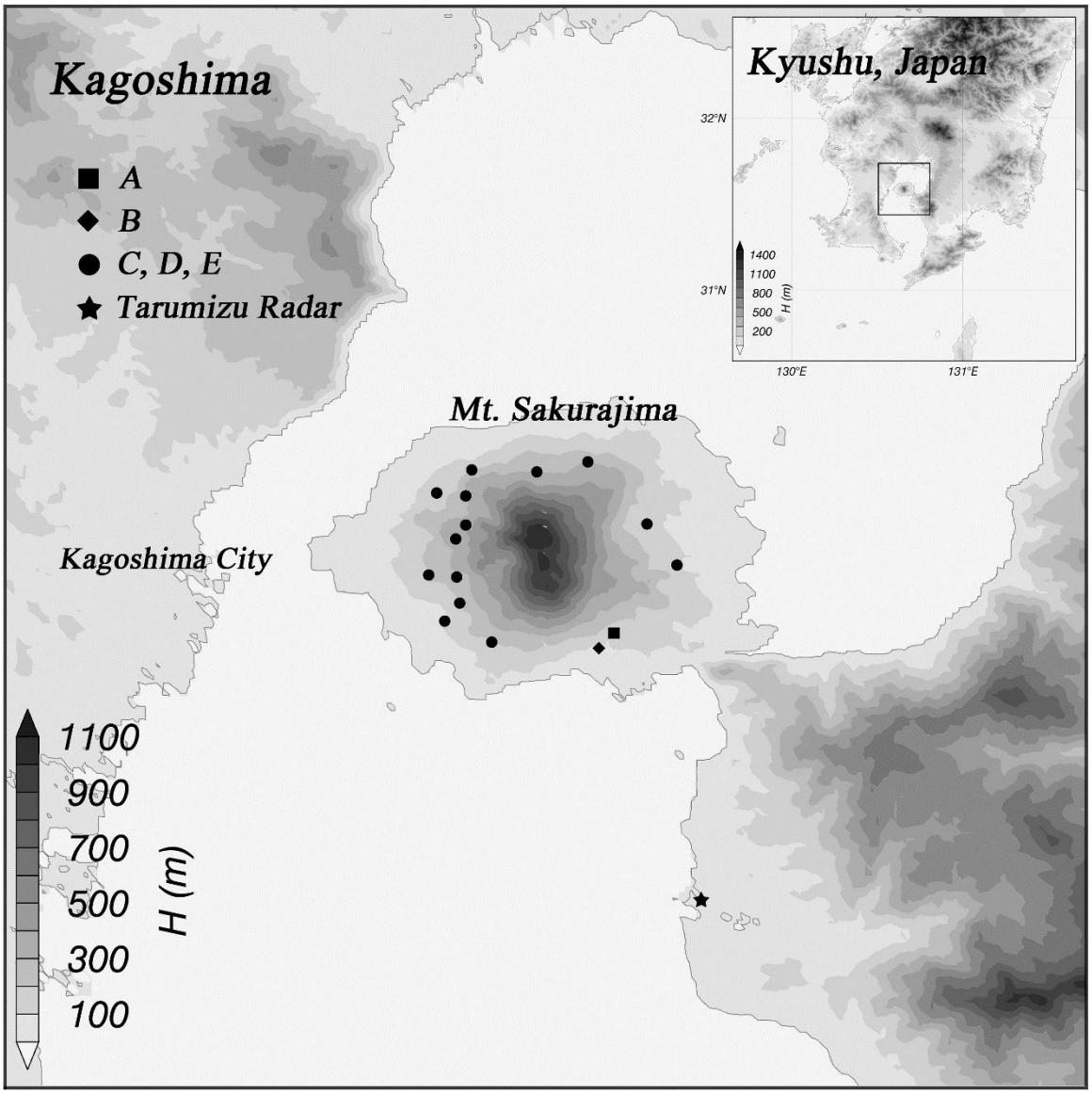

Figure 3. The locations of tephrometers and Showa crater on Sakurajima volcano, Japan. Black symbols indicate the locations of tephrometers and the star, square, and circle symbols correspond to datasets A, B and C–E, respectively. The white circle symbol represents the location of Showa crater.

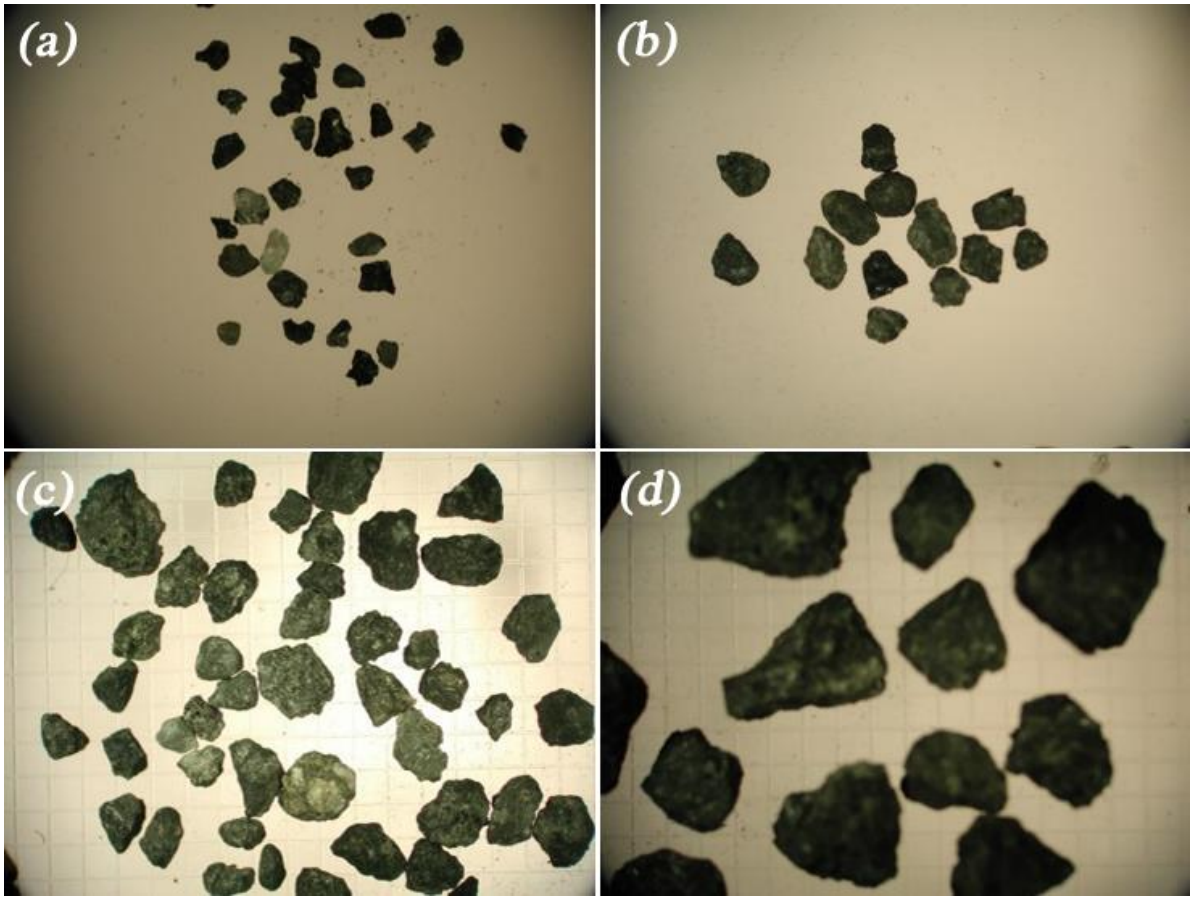

Figure 4. Real images of volcanic ash particles used in the present study. The particles were classified as (a) 0.125 mm < D ≤ 0.25 mm, (b) 0.25 mm < D ≤ 1 mm, (c) 1 mm < D < 2 mm, and (d) 2 < D ≤ 4 mm.

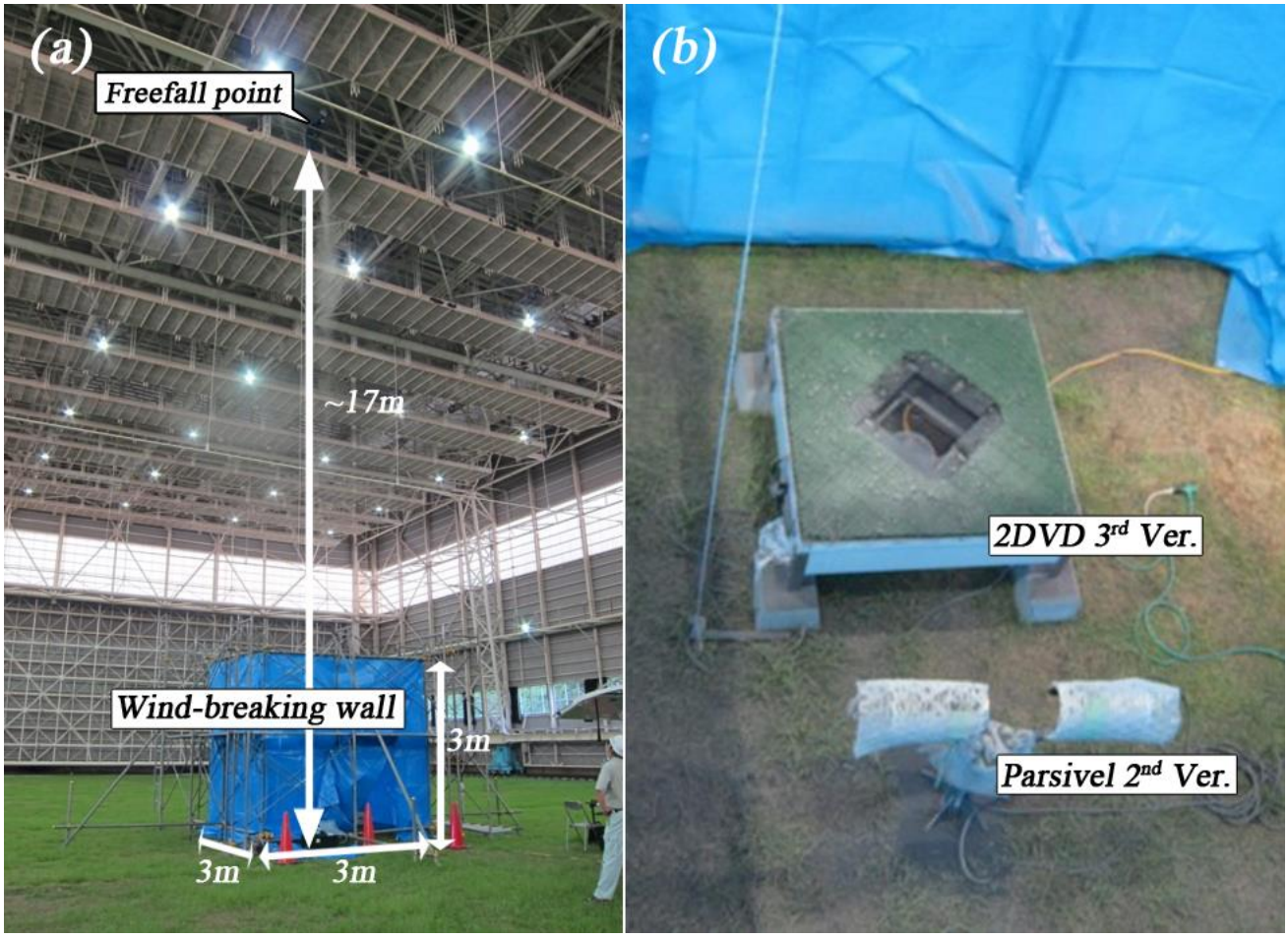

Figure 5. Free-fall experiment conditions of volcanic ash particles on the (a) outside and (b) inside of the wind-breaking wall covering the disdrometers in the large-scale rainfall simulator of the National Research Institute for Earth Science and Disaster Prevention (NIED).

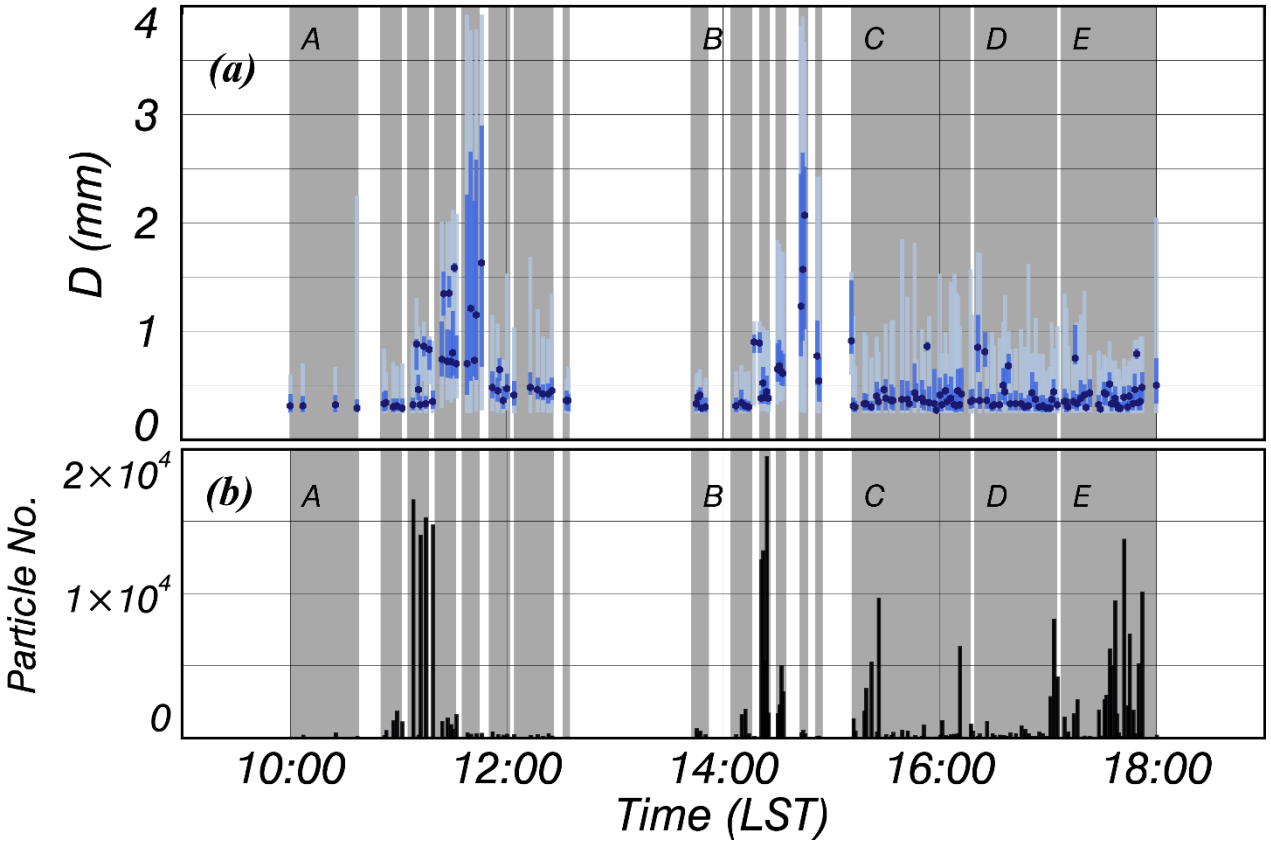

765

766 Figure 6. The 1-min interval time series of D and the number of particles in the free-fall

767 experiment conducted at the NIED.

768

769

770

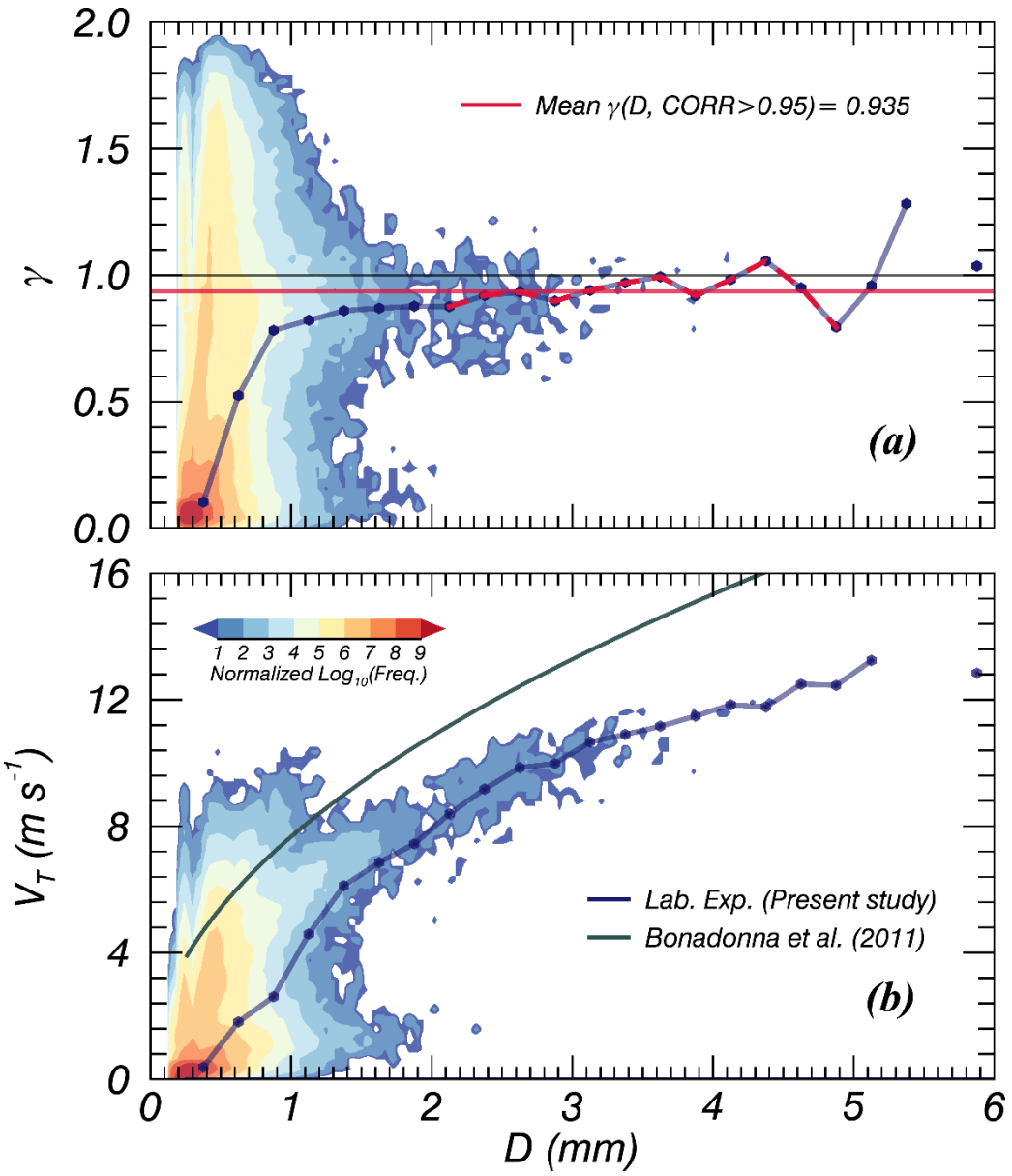

Figure 7. Contour image of volcanic ash particles for (b) the axis ratio (γ) and (b) terminal velocity (V_T) with respect to the sample. The red solid line is the averaged γ satisfying the condition that the correlation coefficient exceeds 0.95. Grey solid line is the relationship of volcanic ash particles suggested by Bonadonna et al. (2011).

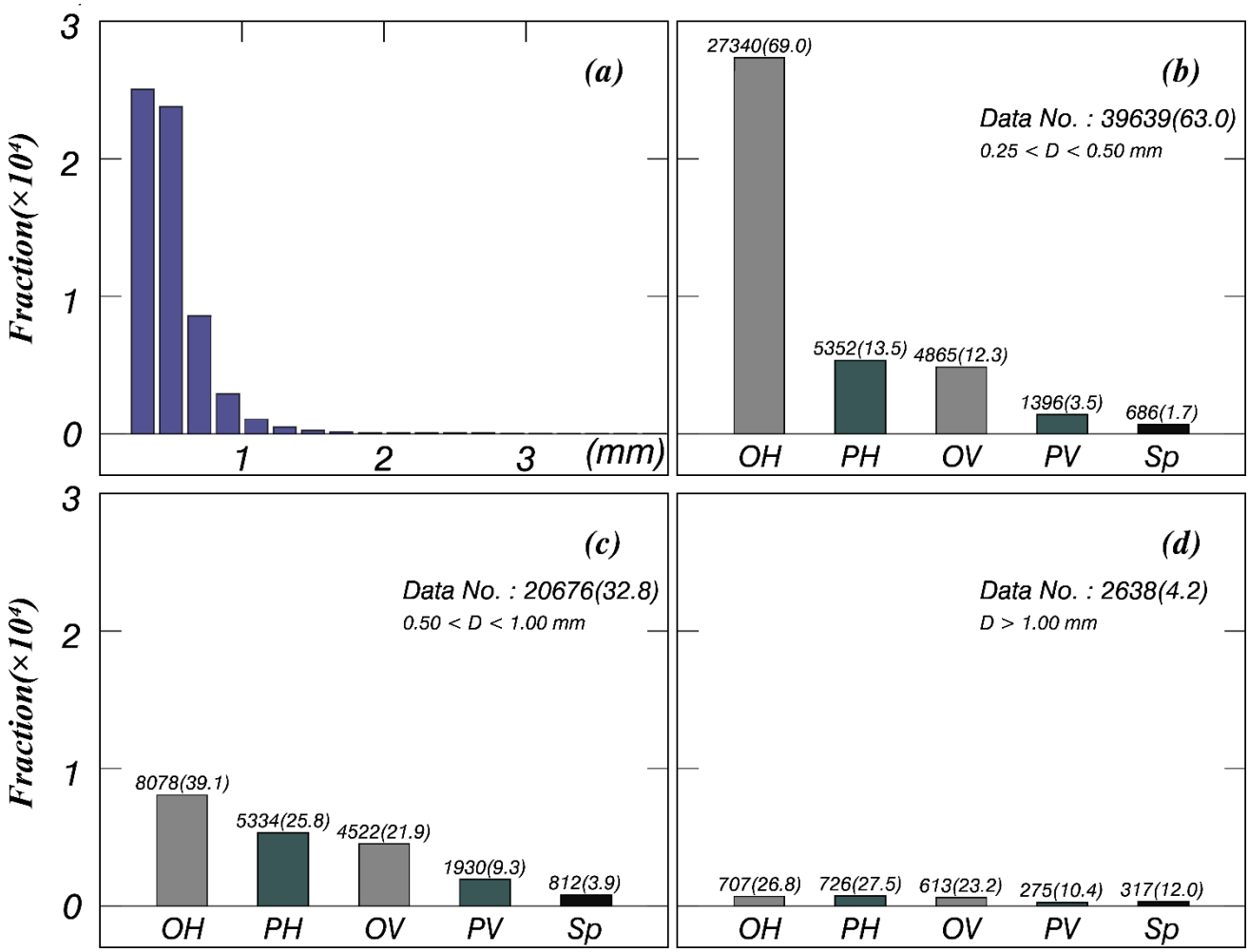

Figure 8. Histograms of volcanic ash particles for (a) all particle types and (b–d) each particle shape type of the phi scale. The grey- and dark grey-shaded (patterned) bars indicate horizontal oblate (OH) (vertical oblate [OV]) and horizontal prolate (PH) (vertical prolate [PV]), respectively. The black bar corresponds to spherical (Sp) particles. The number on the top of each bar plot is the number of data points and that in parenthesis is the percentage for each phi scale.

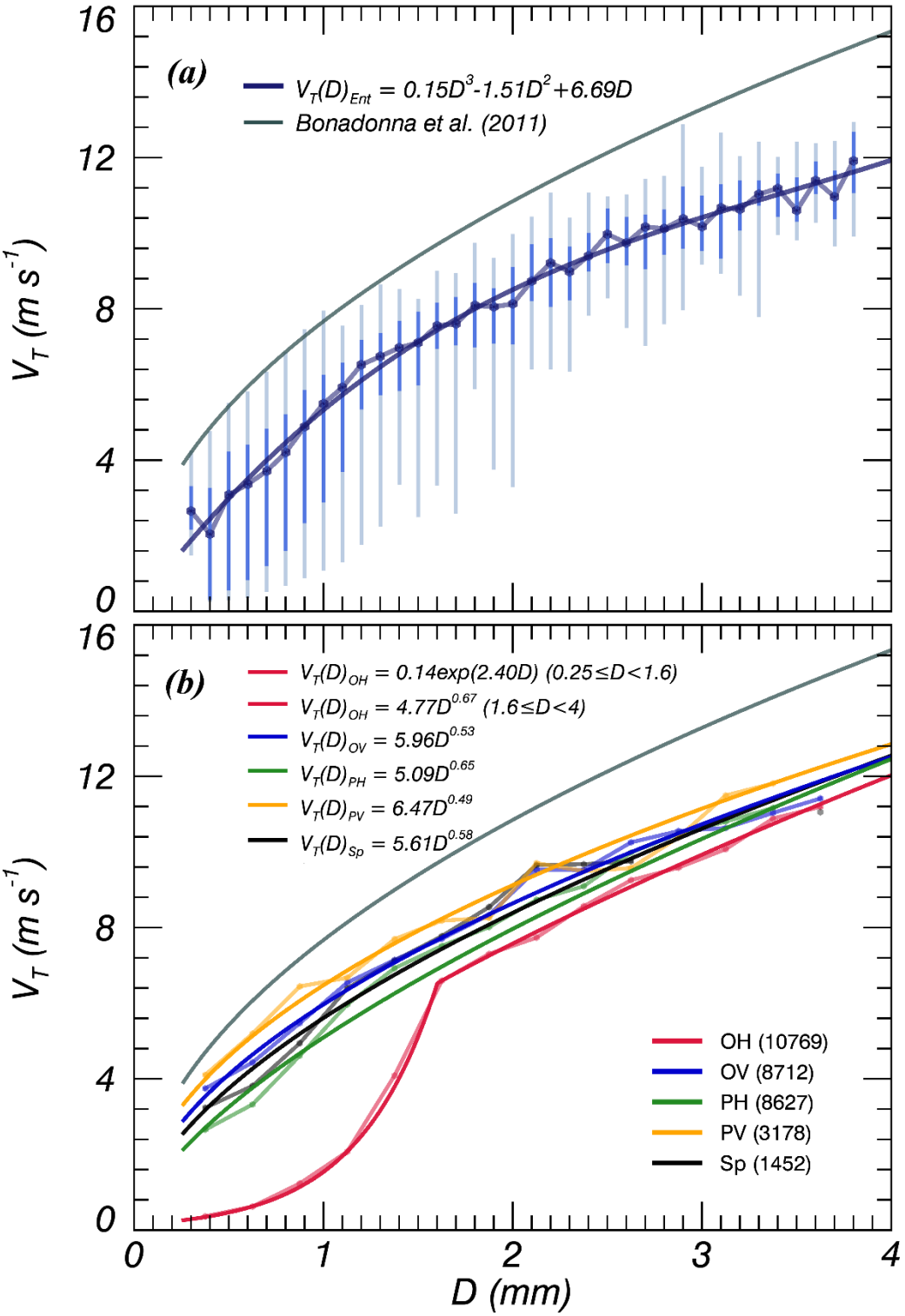

Figure 9. Distribution of (a) quartile and (b) median terminal velocity (V_T) values after applying the 60% V_T QC threshold for all and each individual particle shape type, respectively. The grey solid line shows the relationship of volcanic ash particles suggested by Bonadonna et al. (2011).

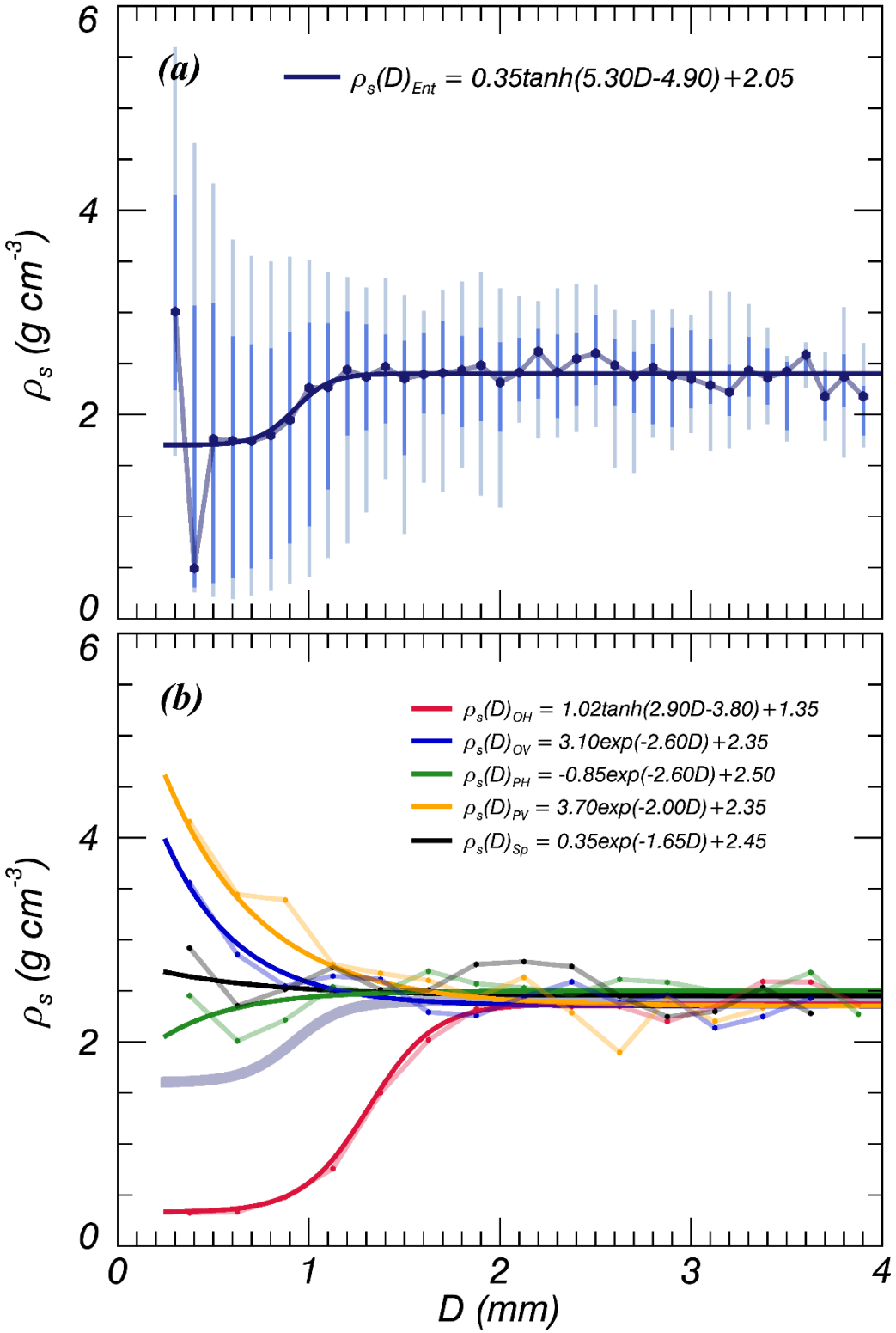

Figure 10. Same as Fig. 9 but for particle density (ρ_s).

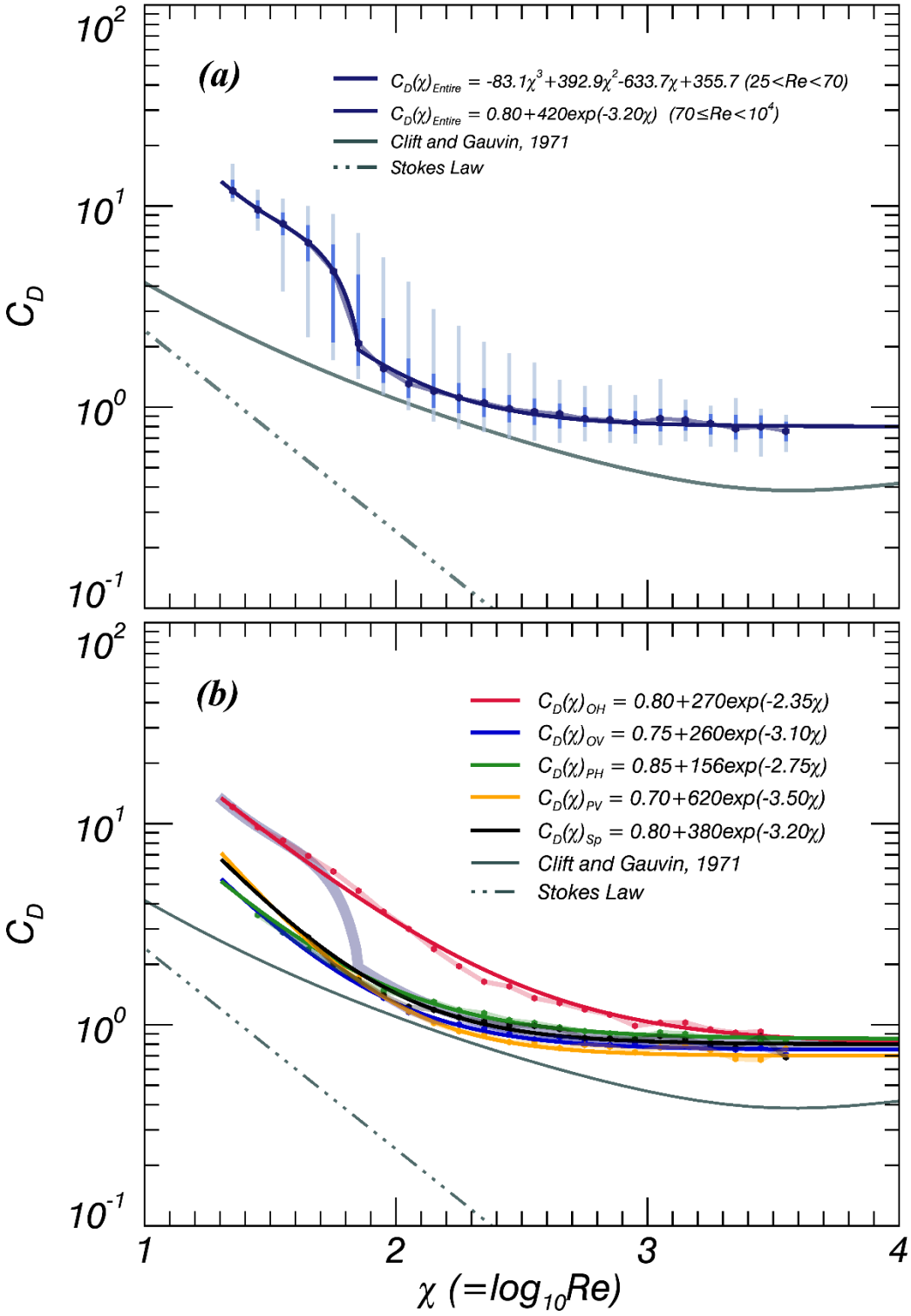

Figure 11. Same as Fig. 9 but for Reynolds number (Re) and drag coefficient (C_D). The grey solid and broken lines in (a) are the relationships of spheres suggested by Clift and Gauvin (1971) and Stokes (1851), respectively.

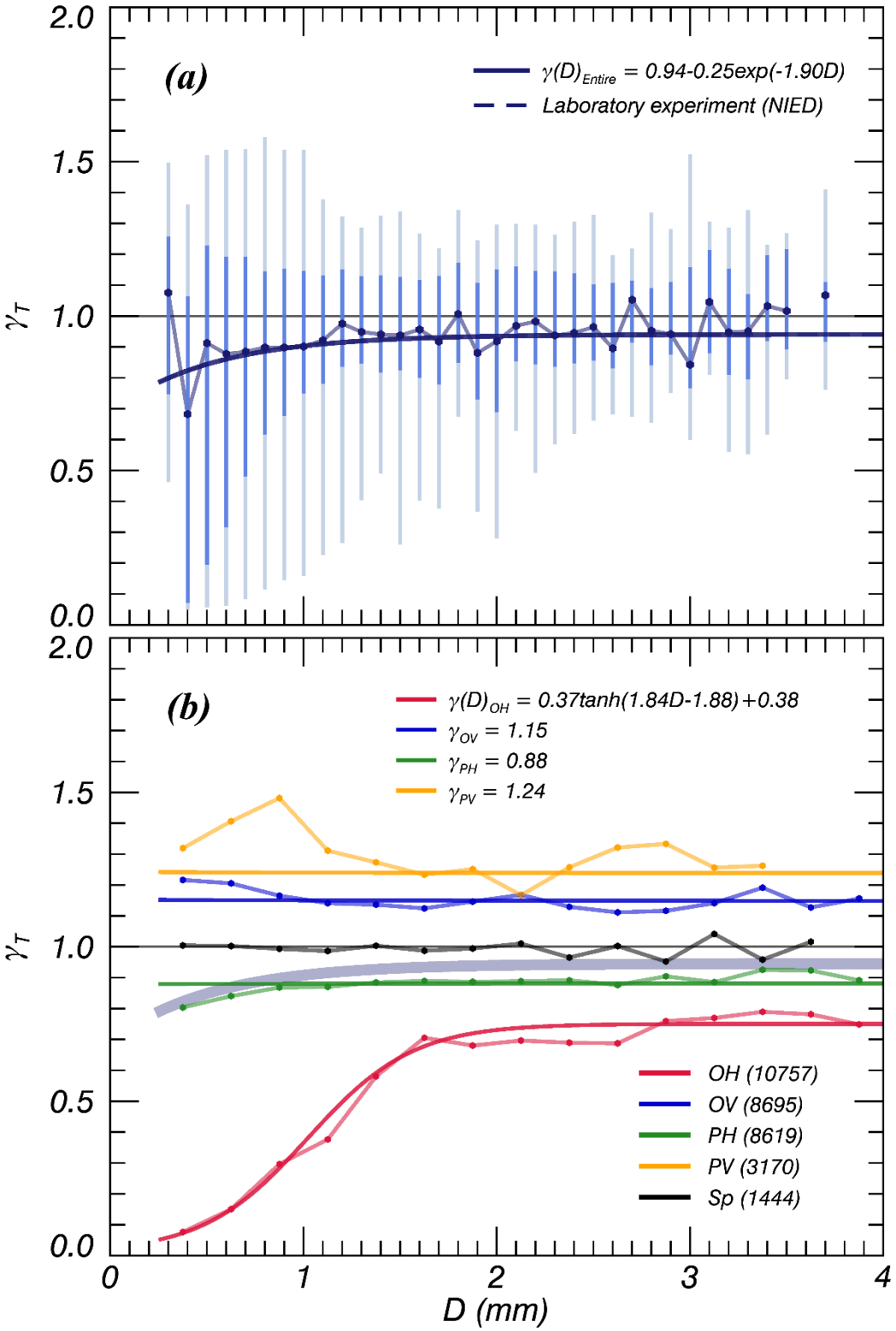

Figure 12. Same as Fig. 9 but for γ.

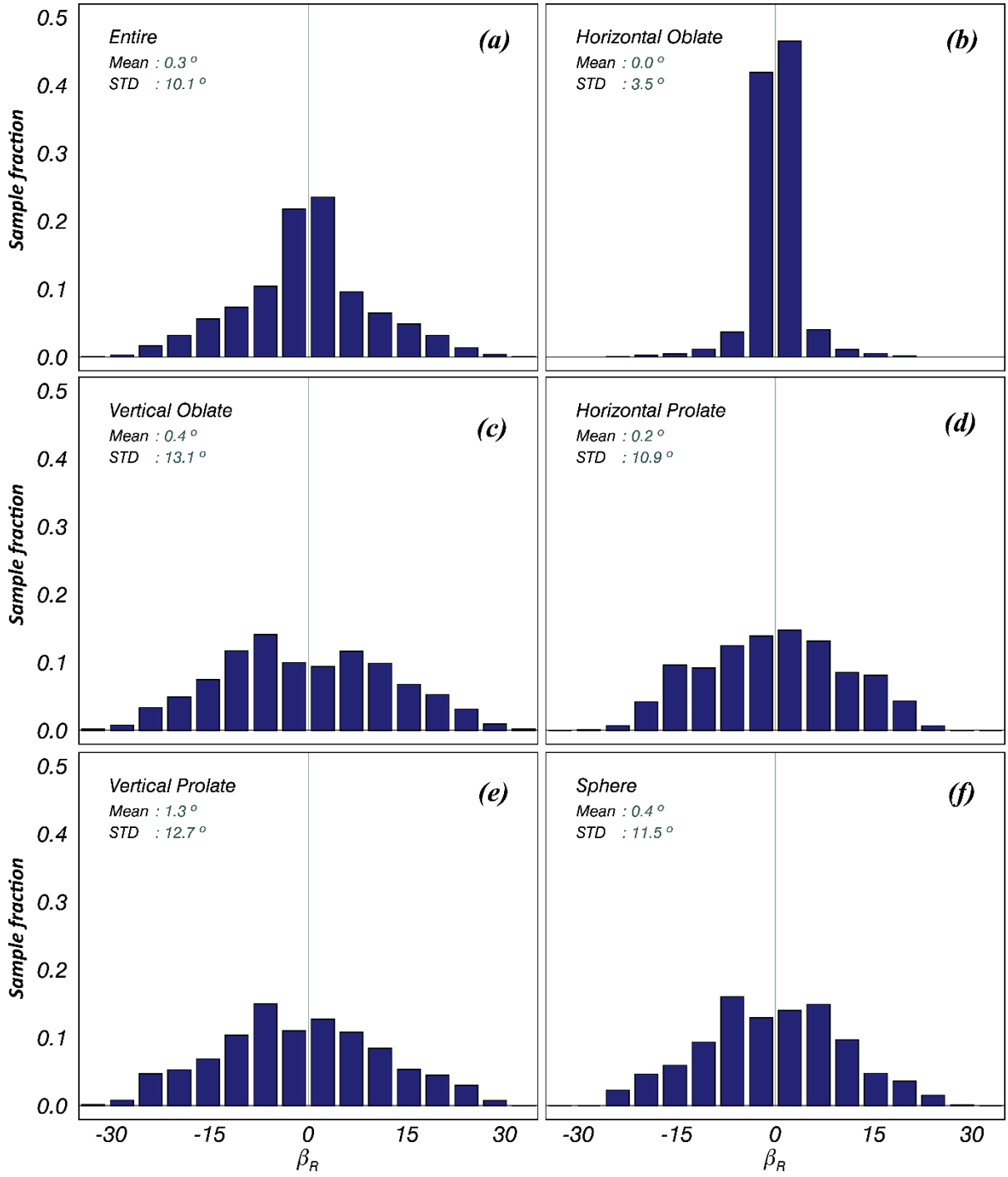

803

804 Figure 13. Histograms of representative canting angle (β_R) for each particle shape type, including

805 the data for all particles.

806

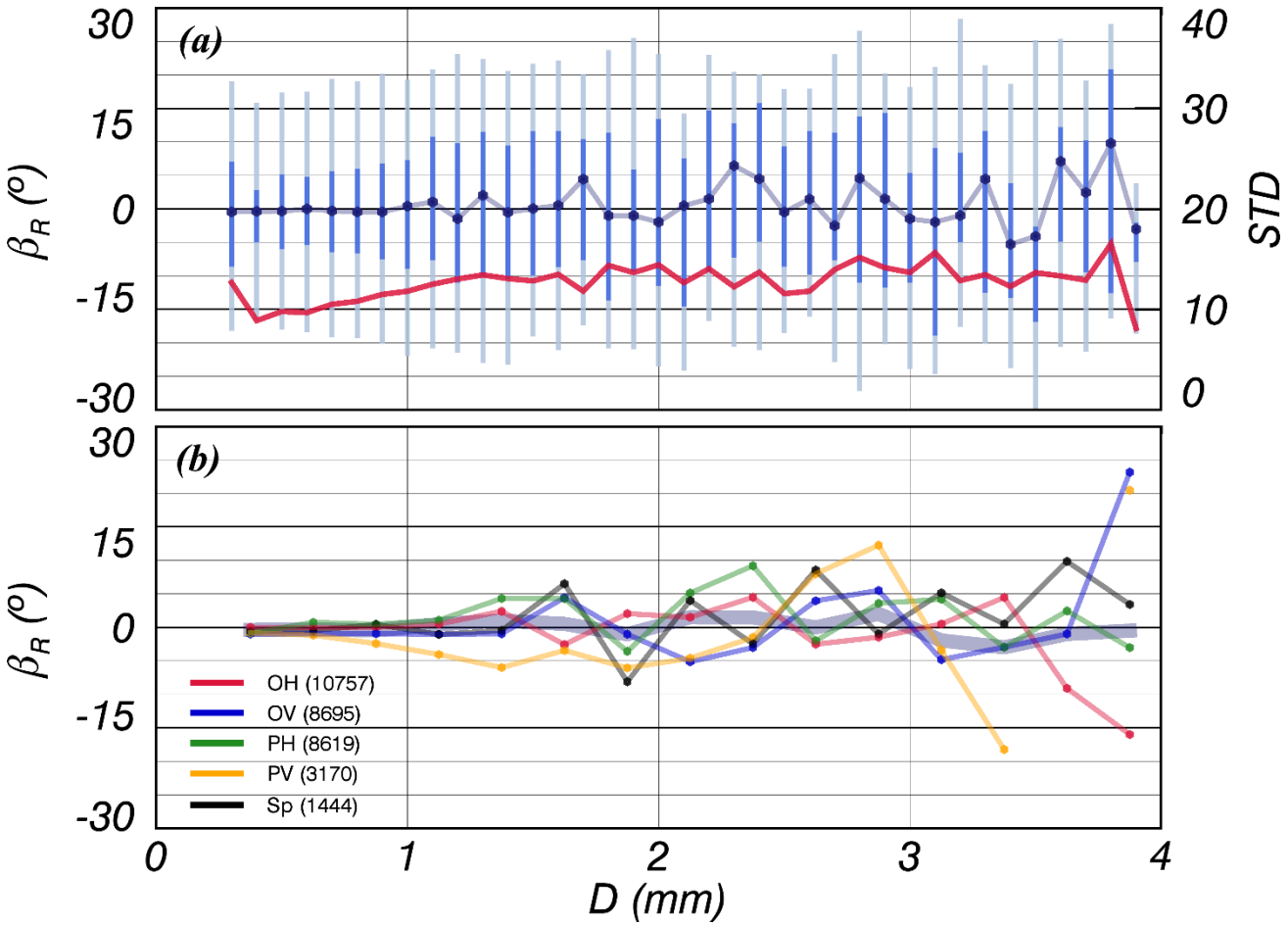

Figure 14. Distribution of β_R with D for each particle shape type including the data for all particles. The red solid line indicates the standard deviation.

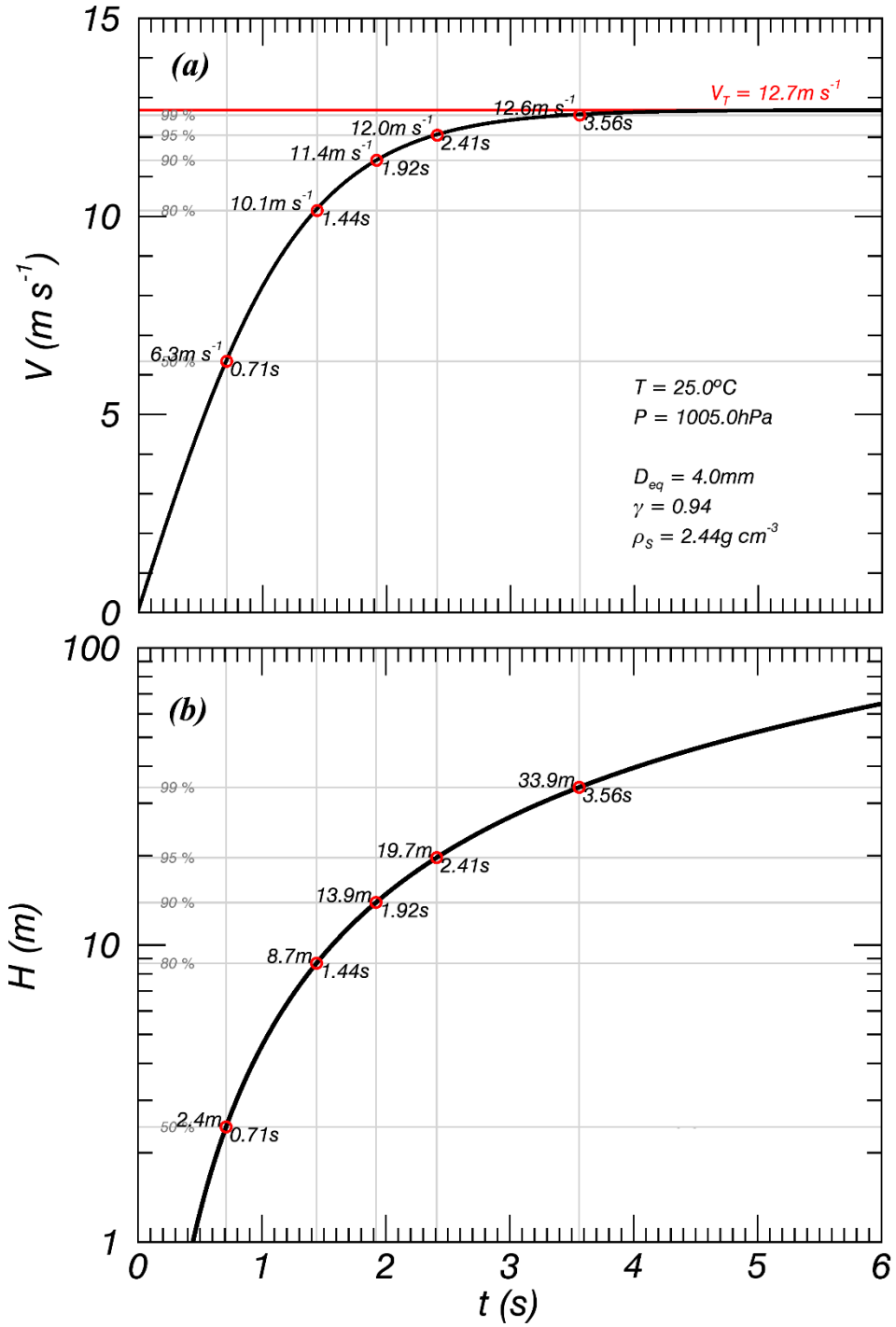

Figure A1. Theoretical (a) fall velocity and (b) falling height for a spheroid with D = 4 mm, considering the surface roughness coefficient of the volcanic ash particle (1.07^{-1}) relative to its fall velocity (Bagheri and Bonadonna, 2016).

818 # Tables

819

820 Table 1. Ash particle classification criteria.

Type	Description	Classification conditions
OH	Horizontal oblate	$\gamma_{T1(2)} < 0.9$ $\lvert\gamma_{T1} - \gamma_{T2}\rvert \leq 0.1\gamma_T$
OV	Vertical oblate	$0.9 \leq \gamma_{T1(2)} \leq 1.1$, $\gamma_{T2(1)} > 1.1$
PH	Horizontal prolate	$\lvert\gamma_{T1} - \gamma_{T2}\rvert > 0.1\gamma_T$
PV	Vertical prolate	$\gamma_{T1(2)} > 1.1$ $\lvert\gamma_{T1} - \gamma_{T2}\rvert \leq 0.1\gamma_T$
Sp	Sphere	$0.9 \leq \gamma_{T1(2)} \leq 1.1$ $\lvert\gamma_{T1} - \gamma_{T2}\rvert \leq 0.1\gamma_T$

821

822 Table 2. Information on the collected volcanic ash particles.

Data	Collection date	Period of free fall experiment (June 18, 2014)	Condition of free fall
A	Dec. 1–31 2008	10:00–12:34 (154 min)	Size by size (phi scale)
B	Mar. 1–31 2010	13:43–14:53 (70 min)	Size by size (phi scale)
C	Feb. 28, 2014	15:11–16:17 (66 min)	Mixed
D	Mar. 31, 2014	16:19–17:05 (46 min)	Mixed
E	Apr. 30 2014	17:07–18:00 (53 min)	Mixed

823

824

825 Table 3. Relationships of terminal velocity with the number of data points, the value of the
826 correlation coefficient (CC) and the root mean square error (RMSE) after applying the 60% V_T QC
827 threshold for each particle shape type.

Type	Data number (%)	Relationship ($0.25 < D$ (mm) ≤ 4)	CC	RMSE
All	32685 (100)	$V_T(D) = 0.15D^3-1.51D^2+6.69D$	0.56	1.22
OH	10757 (33)	$V_T(D) = 0.14\exp(2.40D)$ $(0.25 \leq D < 1.6)$ $V_T(D) = 4.77D^{0.67}$ $(1.6 \leq D < 4)$	0.94	0.46
OV	8695 (27)	$V_T(D) = 5.96D^{0.53}$	0.75	0.85
PH	8619 (26)	$V_T(D) = 5.09D^{0.65}$	0.87	0.74
PV	3170 (10)	$V_T(D) = 6.47D^{0.49}$	0.71	0.96
Sp	1444 (4)	$V_T(D) = 5.61D^{0.56}$	0.91	0.78

828